SCIENCE CHINA
Chemistry

•INVITED REVIEWS•

February 2020 Vol.63 No.2: 149–181
https://doi.org/10.1007/s11426-019-9655-0

Photocatalysis: an overview of recent developments and technological advancements

Yuanxing Fang[1], Yun Zheng[2], Tao Fang[3], Yong Chen[3], Yaodong Zhu[3], Qing Liang[3], Hua Sheng[4,5], Zhaosheng Li[3*], Chuncheng Chen[4,5*] & Xinchen Wang[1*]

[1]*State Key Laboratory of Photocatalysis on Energy and Environment, College of Chemistry, Fuzhou University, Fuzhou 350116, China;*
[2]*Key Laboratory of Molecular Designing and Green Conversions, Fujian Province University, College of Materials Science and Engineering, Huaqiao University, Xiamen 361021, China;*
[3]*Collaborative Innovation Center of Advanced Microstructures, National Laboratory of Solid State Microstructures, College of Engineering and Applied Sciences, Nanjing University, Nanjing 210093, China;*
[4]*Key Laboratory of Photochemistry, CAS Research/Education Center for Excellence in Molecular Sciences, Institute of Chemistry, Chinese Academy of Sciences, Beijing 100190, China;*
[5]*University of Chinese Academy of Sciences, Beijing 100049, China*

Received September 26, 2019; accepted November 19, 2019; published online December 30, 2019

Photocatalysis, which is the catalyzation of redox reactions via the use of energy obtained from light sources, is a topic that has garnered a lot of attention in recent years as a means of addressing the environmental and economic issues plaguing society today. Of particular interest are photosynthesis can potentially mimic a variety of vital reactions, many of which hold the key to develop sustainable energy economy. In light of this, many of the technological and procedural advancements that have recently occurred in the field are discussed in this review, namely those linked to: (1) photocatalysts made from metal oxides, nitride, and sulfides; (2) photocatalysis via polymeric carbon nitride (PCN); and (3) general advances and mechanistic insights related to TiO_2-based catalysts. The challenges and opportunities that have arisen over the past few years are discussed in detail. Basic concepts and experimental procedures which could be useful for eventually overcoming the problems associated with photocatalysis are presented herein.

photocatalysis, carbon nitride, metal oxides, metal nitride, metal sulfide, mechanism, TiO_2

Citation: Fang Y, Zheng Y, Fang T, Chen Y, Zhu Y, Liang Q, Sheng H, Li Z, Chen C, Wang X. Photocatalysis: an overview of recent developments and technological advancements. *Sci China Chem*, 2020, 63: 149–181, https://doi.org/10.1007/s11426-019-9655-0

1 Introduction

Due to the worsening energy crisis and environmental issues plaguing modern society, scientific interest in the development of sustainable resources and cutting-edge industrial processes have increased exponentially, especially within the last two decades. This is exemplified in Figure 1(a), in which the number of scientific publications rose from 1,000 in 1998 to more than 20,000 in 2018. Topics relevant to the use of solar radiation as a primary energy resource are of particular interest in the field given the extent of its global impact and its importance to the lives of billions of people [1]. A typical example of this is the process of photosynthesis, which is fundamental in the immobilization and conversion of solar energy into chemical resources (mainly its conversion into carbohydrates) as sustenance for higher animals. These natural processes serve as inspiration for researchers seeking

---

*Corresponding authors (email: zsli@nju.edu.cn; ccchen@iccas.ac.cn; xcwang@fzu.edu.cn)

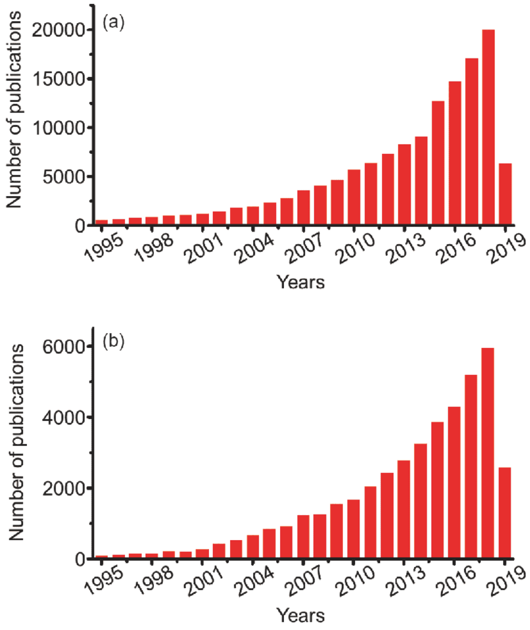

Figure 1 The number of scientific publications on topics related to (a) sustainability and (b) photocatalysis. Source: Web of Science (color online).

to mimic these results via artificial means, namely photocatalysis.

Of particular interest is the use of photocatalysis as a means of accelerating redox reactions in the presence of catalysts and solar energy. These processes were first described in the 1960s, in which photoinduced phenomena were investigated using semiconducting solids, such as TiO_2 and ZnO [2]. At that time, a few small molecules were found to be adsorbed or desorbed from the surface of the solid semiconductor under ultraviolet (UV) light irradiation. The band theory governing semiconductors was used explain these phenomena and is now crucial for our understanding of the fundamentals of photocatalysis. One key milestone in history was the discovery made by Honda and Fujishima [3] in 1972; their work focused on the use of a TiO_2-based photoanodes for the production of oxygen and hydrogen gases via water-splitting reactions under UV light. This report was a turning point in the research, as it showed that redox reactions could be initialized on the surface of the semiconductor via solar illumination. Half a century later, the applications for photocatalysis have been extensively expanded to include CO_2 and N_2 fixations, methane activation, and organic synthesis [4–10]. The mechanisms by which these reactions occur have also received increased attention from the scientific community over the years (Figure 1(b)). In light of the boom in scientific publications on these topics, there is an urgent need to review recent advances in photocatalysis so as to maintain a clear overview of the current state of things in the field.

In the last decade, several comprehensive reviews were presented on this topic. Albini *et al.* [11] reviewed multifaceted concepts of photocatalysts for green chemistry applications. Chai *et al.* [12] focused on the use of polymeric carbon nitride (PCN) for photocatalysis. Zhao *et al.* [13] chose to highlight the use of heterogeneous visible-light photocatalysis for selective organic transformations. In recent years, the field has seen significant progress as increasingly more visible-light active materials have been developed for a wide variety of potential applications. Despite these advances, these new visible-light active materials are still plagued with performance issues, namely those influenced by processes such as transfer and surface activity as well as charge separation. Several comprehensive studies have been conducted on finding ways to overcome these limitations. Since 2009, the use of PCN photocatalysts in real-world applications has been of great interest to researchers [14–16]. PCNs are wonderful candidates for sustainable, renewable energy applications as they possess excellent chemical and physical stability. Countless studies have attempted to gain the insights into the photocatalytic mechanism through which PCNs exert their influence.

In this review, the technological and procedural advancements recently made in the study of photocatalytic processes are categorized into three sections: (1) catalyzation of redox reactions via visible-light-sensitive metal-based photocatalysts; (2) PCN photocatalysis; and (3) mechanistic pathways seen in semiconductor photocatalysis. In addition to the current challenges and future opportunities in the field, experiments and essential concepts which may be useful for overcoming these problems are also presented.

2 Metal oxides/nitride/sulfide photocatalysts

Recent developments, including the use of metal oxides, nitrides and sulfides as photocatalysts are presented in this section. Since the performances of many known visible-sensitive photocatalysts today are often plagued by issues related to charge diffusion length and surface redox activity, this section aims to analyze the progress made in overcoming these limitations. In addition, several traditional metal-based photocatalysts that are used in advanced photocatalytic applications, namely as the use of TiO_2 for CO_2 fixation, will also be reviewed.

2.1 Iron-based materials

Hematite (α-Fe_2O_3), a naturally-occurring iron-based material commonly available, has been extensively studied for its use in photocatalytic water-splitting reactions. Compared to other materials, hematite stands out due to its abundance, non-toxicity, and excellent photochemical stability. There is evidence to indicate that hematite has a sufficient valence edge and a band gap of ca. 2.0 eV which, theoretically, has a photo-response at low bias. In comparison to the photo-response associated with reversible hydrogen electrodes (RHEs), hematite's photo-response often occurs at 0.4 V before quickly plateauing at a photocurrent density of 13 mA/cm^2. Unfortunately, the performance of α-Fe_2O_3 under practical conditions is severely hindered by several issues, including the occurrence of surface states recombination, slow water oxidation kinetics, poor majority carrier conductivity (electron mobility $\mu_e \approx 0.01$ cm^2/(V s), electron concentration $n_e \approx 10^{18}$ cm^{-3}), a low absorption coefficient ($\alpha^{-1} \approx 120$ nm when $\lambda = 550$ nm) caused by indirect transition processes, and the short diffusion length seen in minority carriers (≈2 nm) [17].

In this review, recent research efforts toward finding solutions for these drawbacks are presented, including improvements made to the surface state recombination process, better oxygen evolution rate (OER) kinetics, and the use of bulk recombination for α-Fe_2O_3 photoanodes. Another highlight of this section focuses on other iron-based materials, like β-Fe_2O_3 and spinel ferrites.

2.1.1 Improvements in surface state recombination and OER kinetics of hematite photoanodes

Surface states are localized states with energies distributed across the band gap that are deposited on the surface of a semiconductor [18]. It is generally accepted that surface states are key in determining the PEC performance of hematite photoanodes. Previous studies have shown that surface states influenced the OER kinetics of hematite in three main ways. In this section, we discussed these roles and investigated several methods that were used to modify the surface of α-Fe_2O_3.

In one study, it was shown that surface states directly participated in the OER mechanism. Bisquert *et al.* [19] employed impedance spectroscopy to systematically confirm the presence of surface states via a capacitive process in which the OER mechanism was initiated as the surface states were discharged and the charge-transfer resistance was decreased. As observed, the water oxidation step took place via surface states rather than via the valence band top (Figure 2(a)). The chemical identity of these kinds of surface states was further investigated [20–23] (Figure 2(b)), and it was eventually confirmed that the trapped Fe(III)-OH groups turned into Fe(IV)=O; this direct evidence was acquired via operando infrared (IR) spectroscopy conducted by Hamann *et al.* (Figure 2(c, d)) [24]. Another well-known effect of surface states was the pinning of the Fermi level since this promoted bulk and surface recombination. When there was an excess in the number of surface states, any increase in applied bias served to charge the Helmholtz layer instead of increasing the bending degree observed in the space-charge layer [25]. Meanwhile, other studies found that surface states were also acted as recombination centers for photogenerated

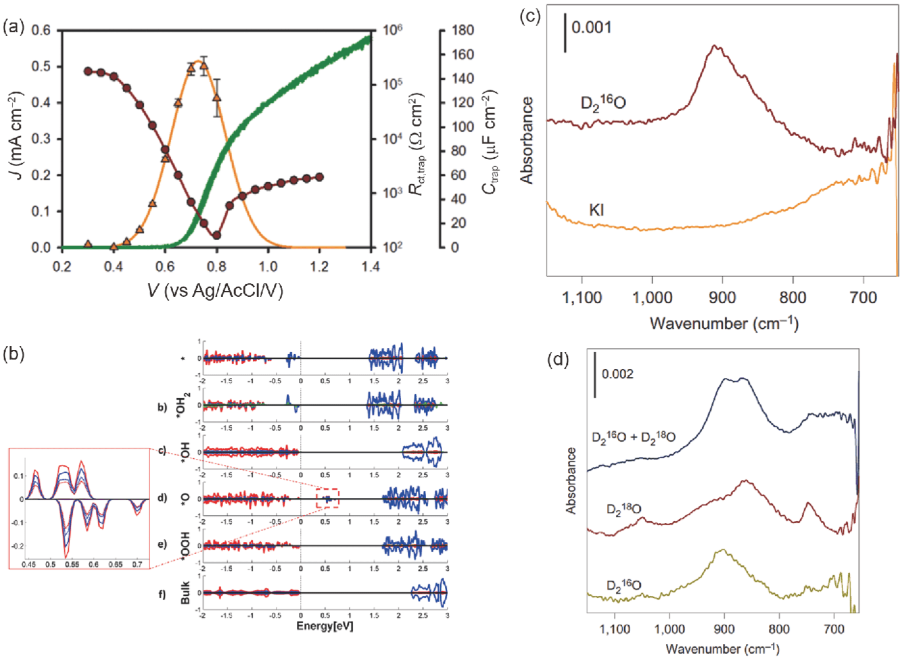

Figure 2 Evidence that surface states were directly involved in the OER mechanism with chemical origin as Fe(IV)=O groups. (a) *J*-*V* curve (green line), C_{trap} (the surface states capacitance, orange triangles), and $R_{ct,trap}$ (the resistance that was transferred through carriers via surface states, red circles) values under different bias; (b) DFT+U calculations confirmed that the surface state's chemical identity was Fe(IV)=O; (c) operando IR spectra conducted with/without a hole scavenger (KI) suggested that the peak at 898 cm^{-1} was an intermediate species involved in the water oxidation process; (d) using isotope labeling, the peaks at 898 and 857 cm^{-1} were assigned to Fe=^{16}O and Fe=^{18}O, respectively, as the chemical origin of the surface states participating in the OER mechanism. Reproduced with permission from Ref. [19]. Copyright (2008) American Chemical Society (color online).

electron-hole pairs [26,27]. It should be noted that there are various sources of surface states, including dangling bonds, adsorbed groups, etc. Hence, depending on the specific type of surface state present in the experiment, not all of these three effects would be revealed.

As far as we know, the only way to improve the surface states of a photoanode is to passivate them. The presence of overlayers, such as Al_2O_3, Ga_2O_3, ZnO or SiO_x, served to reduce the number of surface states and achieve a preferable onset potential and photocurrent [28–31]. Hydrothermal regrowth was another strategy employed to passivate surface states of hematite photoanodes. Wang and co-workers [32] used this method to decrease short-range disorder near the hematite's surface, which led to a reduction in the onset potential by about 400 mV (Figure 3). Furthermore, a $NiFeO_x$ passivation layer was applied in order to achieve a lower onset potential (0.45 V) when compared to the potential observed in RHEs. Other methods of passivation, including high-temperature annealing and salt/acid treatments, served to improve the performance of a hematite photocatalysts by removing the surface states altogether [33–35].

Surface oxidation kinetics were shown to compete with surface states recombination. The sluggish water oxidation kinetics observed on hematite severely hampered surface recombination. Interestingly, the surface states may be responsible for the slow reaction kinetics in the first place due to the reasons discussed above. Even though the mechanism by which OER kinetics transpired on the hematite remains unclear, deposition of an electrocatalyst or co-catalyst was considered as an effective method for accelerating surface reaction kinetics. Co-Pi, IrO_2, Co_3O_4, and NiOOH have been nominated as good choices for this purpose in several studies [27,36–38].

2.1.2 *Improvements for bulk recombination of hematite photoanodes*

Another contributor to the low solar-to-hydrogen conversion efficiency of hematite was the occurrence of bulk recombination arising from an extremely short hole diffusion length and the poor conductivity of the major carrier. However, significant progress has been achieved in the past decade. To this end, both nanostructure and heterojunction engineering as well as substitutional doping techniques have become effective strategies for enhancing the bulk charge separation efficiency.

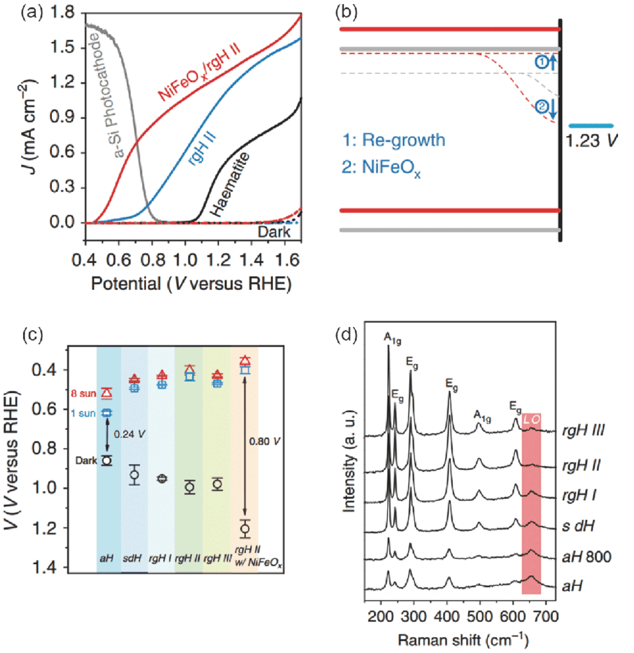

Figure 3 Passivating surface states and reducing Fermi-level pinning through regrowth treatment and the application of a $NiFeO_x$ overlayer. (a) *J-V* curves of hematite photoanodes with various surface modifications; (b) band diagram of the unmodified hematite photoanode (gray line) and the $NiFeO_x$/rgH II hematite photoanode (red line) under flat-band, quasi-equilibrium conditions; (c) open circuit potential tests of various hematite photoanodes under 8-sun (red, triangle), 1-sun (blue, square), and dark (black, circle) conditions; (d) Raman shift spectra of various hematite photoanodes showing reduction of the surface states after being subjected to the regrowth treatment. Reprinted from Ref. [32] with permission. Copyright (2015) Springer Nature (color online).

Substitutional doping with tetravalent cations (Si^{4+}, Ti^{4+}, Sn^{4+}, etc.) was shown to increase the electron concentration in hematite samples. For example, Lee *et al.* [39] fabricated Ti-doped Fe_2O_3 via a hydrothermal method that resulted in a plateau photocurrent of 3.76 mA/cm^2, a value which was 2.5 times higher than that observed for the undoped photoanodes. This improvement was partially ascribed to increased donor density in hematite by Ti doping; this observation was noted in other reports as well [40,41]. Doping was also shown to improve the PEC performance of hematite by tuning morphology [42], creating lattice distortion [43], boosting electron mobility [44], and enhancing light absorption [45]. Representative doped hematite photoanodes are listed in Table 1 below [46–50].

Nanostructure engineering was shown to be a silver bullet when it comes to the trade-off between poor light absorption and a short hole diffusion path. Using a specific processing method or template, it was possible to shape hematite photoanodes into different nanostructures such as nanorods, nanotubes, nanosheets, and core-shells. When compared to more compact panel electrodes, these nanostructured photoanodes exposed more cut-off points and surfaces which were favorable for light harvesting, surface catalytic activity, and carrier transportation. Wang *et al.* [51] employed an anodization method for the preparation of vertically grown hematite nanosheet films. Modified with Ag nanoparticles and Co-Pi, this photoanode exhibited a remarkably high photocurrent of 4.7 mA/cm^2 at 1.23 V vs. RHE (Figure 4) [51].

Studies found that combining hematite and other semi-

Table 1 Hematite photoanodes generated using substitutional doping

Synthesis	Photoanode structure	V_{on} a) (V vs. RHE)	$J_{1.23\ V}$ b) (mA/cm^2)	$J_{plateau}$ (mA/cm^2)	Ref.
APCVD	fractal-like cauliflower Si:Fe_2O_3/IrO_2	0.85	3.2	3.6	[36]
Hydrothermal	urchin-like Ti:Fe_2O_3 nanorods	1.00	1.9	3.6	[39]
Hydrothermal	porous Ti:Fe_2O_3/SiO_x/Ti-FeOOH	0.85	4.1	5.8	[46]
Hydrothermal	Sn:Fe_2O_3 nanocorals	0.90	2.0	2.9	[42]
Hydrothermal	Ru:Fe_2O_3 nanorods	0.71	5.7	6.4	[44]
Hydrothermal	wormlike Pt:Fe_2O_3/Co-Pi	0.70	4.3	6.5	[47]
Hydrothermal	P:Fe_2O_3 nanowires/ Co-Pi	0.80	3.1	4.5	[48]
PECVD	coarse-grained In-Sn:Fe_2O_3	0.80	2.5	3.8	[49]
Hydrothermal	F:Fe_2O_3 nanocrystals	0.70	2.5	3.1	[45]
Hydrothermal	Fe_2O_3 nanowires with O vacancies	1.00	1.8	3.5	[50]

a) The potential at which the tangent to the *J-V* curve with a maximum slope intersected the horizontal axis. b) The photocurrent under the applied bias of 1.23 V vs. RHE. All readings were performed under pH 13.6 and at an irradiation intensity of 100 mW/cm^2.

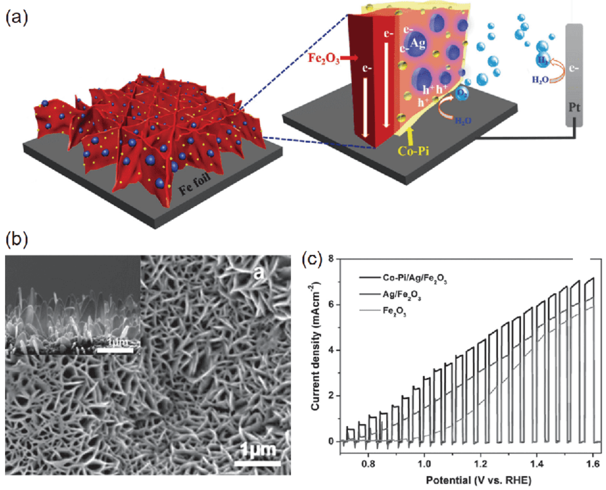

Figure 4 (a) Schematic of vertically grown hematite nanosheets modified with Ag nanoparticles and Co-Pi; (b) SEM surface view of this Fe_2O_3 film; (c) *J-V* curves of various hematite photoanodes under chopped light illumination in 1 M NaOH. Reprinted from Ref. [51] with permission. Copyright (2016) Wiley-VCH (color online).

conductors with the proper band-edge position was another effective approach for reducing bulk recombination of the photogenerated carriers; this process was called heterojunction engineering. An energy-band-matched heterojunction system induced an internal electric field. Thus, if the field's direction was beneficial for the separation of the photogenerated carriers, bulk recombination was reduced, and the PEC performance of hematite improved. Numerous studies have reported the materials most effective for heterojunction engineering, namely $SrTiO_3$, $MgFe_2O_4$, $ZnFe_2O_4$, WO_3, $LaFeO_3$, and NiO [52–57].

2.1.3 Beta-Fe_2O_3 and spinel ferrites

β-Fe_2O_3, which is a metastable form of an Fe(III)-based oxide, is an economic, n-type, non-toxic material used for the production of photoanodes. Although it undergoes phase transformation at high temperatures, β-Fe_2O_3 is stable enough under PEC reaction conditions. Additionally, β-Fe_2O_3 stands out due to its strong visible absorption band gap (ca. 1.9 eV) and direct light-absorption capacity; its theoretical plateau photocurrent is approximately 17 mA/cm^2. In a study conducted by Li *et al.* [58], pure β-Fe_2O_3 nanoparticle-assembled films were prepared via electrophoretic deposition. The plateau photocurrent was 0.12 mA/cm^2 under illumination with AM 1.5 G simulated sunlight; these results, however, leave plenty of room for improvement in the future. In addition to its ability to split water using solar energy, β-Fe_2O_3 has also been proven to be effective in the photodegradation of organic contaminants [59,60].

Recently, research focus has been geared toward spinel ferrites. These are chemical compounds in the form of MFe_2O_4 (M=Mg, Zn, Ca, Cu, etc.). Traditionally, these materials were utilized as the overlayer for a composite electrode system for solar-driven water splitting and photocatalytic degradation [53,61,62]. Meanwhile, more efforts have been placed in improving the PEC performance of individual spinel-ferrites electrode systems. Taking $ZnFe_2O_4$ as an example, Li and co-workers [63] recently employed a fast and effective spray pyrolysis method to manufacture a Ti-doped $ZnFe_2O_4$ photoanode. In that study, the plateau photocurrent was noted at 0.7 mA/cm^2. Sivula and co-workers [64] found that $ZnFe_2O_4$ photoanodes with more structural disorder exhibited superior photogenerated carrier separation efficiency, with a benchmark photocurrent value of 1.7 mA/cm^2 at 1.6 V vs. RHE. However, despite the positive results and high theoretical plateau photocurrent value (at about 11 mA/cm^2), more extensive research is still needed to determine the factors which limit the performance of $ZnFe_2O_4$ and other iron-based materials.

2.2 TiO_2

Among the numerous photocatalysts reported throughout the literature, TiO_2 stands out as this is the most investigated photocatalyst used for CO_2 fixation reactions. Pure TiO_2 only allows for the absorption of UV light across a large band gap (~3.20 eV) and suffers from fast recombination processes for its photogenerated electron-hole pairs. Except for the compound system which had been constructed, e.g., forming heterostructures and Z-scheme catalytic systems as well as loading co-catalysts, several modifications have been made in an effort to increase visible-light absorption and boost the efficiency of monocomponent TiO_2. These efforts include nanostructuring, metal and non-metal doping, and introducing oxygen vacancies, as well as crystal and facet engineering.

Morphological aspects such as particle size and shape, geometry, and crystalline phase of TiO_2 affected the surface area of a photocatalyst, in particular, the electron transport systems and the mechanism by which mass transfer occurred [65]. Kočí *et al.* [66] synthesized pure TiO_2 particles with crystallite diameters ranging from 4.5 to 29 nm and found that the optimum particle size (14 nm) resulted in the highest yields of CH_4 and CH_3OH; this was attributed to a larger surface area, more efficient charge transfer, and better absorption of light. Other than decreasing the photoanode's particle size, fabricating one-dimensional TiO_2 nanostructures like nanorods, nanotubes, and nanowires, was considered as an effective strategy for enhancing the photocatalytic CO_2 reduction activity brought about by a larger surface area, reduced grain boundaries, and faster diffusion of the reactants [67,68]. Ping and co-workers [69] prepared self-organized TiO_2 nanotube arrays (TNAs) via electrochemical anodization in which CO_2 and H_2O were converted to alcohols under Xenon lamp illumination. Ultrathin anatase TiO_2 nanosheets (2 nm in thickness) exposed with 95% of {100} facets were prepared by Ye's group [70], and were found to be five times more efficient than their cuboid counterparts with 53% of exposed {100} facets for photocatalytic reduction of CO_2 into CH_4. The high photocatalytic activity was ascribed to a larger surface area which automatically provided more active sites, as well as the superior electronic band structure resulting from the higher percentage of exposed {100} facets.

Doping is one of the most widely applied strategies for extending the light-absorption range of a photocatalyst due to its effectiveness in narrowing the band gap in semiconductors [71]. Two ways to dope TiO_2 have been reported, namely metal doping and non-metal doping. For metal doping, Cu, Ni, Ce, and Ag were "doped" into the lattice of TiO_2 to substitute the titanium atoms that were present, thus creating "impurity energy levels" within the band gap; this, in turn, narrowed the band gap and improved photocatalytic activity [72–75]. In non-metal doping, N, C, S or I were used to replace the oxygen atoms in the TiO_2 lattice, thus raising its VB maxima and narrowing its band gap for more efficient utilization of the incident light [76–80].

Studies have shown that oxygen vacancy not only enhanced the visible-light absorption of TiO_2, but also acted as an active site for CO_2. Liu *et al.* [81] had engineered oxygen-deficient, blue TiO_2 nanocrystals with co-exposed {101} and {001} facets (TiO_{2-x}\{001\}–\{101\}) to enhance CO_2 photoreduction under visible light. A relatively high quantum yield (0.31% under UV-vis light and 0.134% under visible light) was noted for the reduction of CO_2 to CO. Possible reasons for this outstanding performance were the exposure of more active sites (e.g., undercoordinated Ti atoms and oxygen vacancies), the relative ease of electron transfer between the {001} and {101} planes, and the formation of a new energy state (Ti^{3+}) within the TiO_2 band gap which extended the photoanode's visible-light response.

To improve performance, some researchers have taken advantage of the energy differences between the various facets. Generally, TiO_2 is comprised of three facets, namely {001}, {010}, and {101}. Due to differences in the geometric configuration, band structure, and surface characteristics, these facets possess different photocatalytic activities. Among the low index facets of {001}, {010}, and {101}, TiO_2 crystals with {010} facets exhibited better photocatalytic performance with higher surface energy [81,82]. Ye *et al.* [83] demonstrated that the photocatalytic activity order in the gaseous phase for the photoreduction of CO_2 to CH_4 was {010}>{101}>{001}. The higher activity of {010} facet was ascribed to increased CO_2 adsorption and more efficient charge separation.

Apart from TiO_2, several perovskite titanates, such as $SrTiO_3$ [84], $PbTiO_3$ [85], and $CaTiO_3$ [86], have also been explored for use as part of a gas phase CO_2 photocatalytic reduction reaction.

2.3 $BiVO_4$

As a ternary metal oxide with a band gap of 2.4 eV, $BiVO_4$ has great potential for extensive application in solar-driven redox reactions. $BiVO_4$ is generally synthesized using the hydrothermal approach, which often leads to the formation of uniform films as the system's photoanode [87]. Nevertheless, there are some key characteristics in bare $BiVO_4$ that prevent it from achieving high potential efficiency, including the presence of adverse charge combinations and slow charge-transfer processes. In the last decade, several strategies have been proposed in an effort to overcome the charge-transfer issues and promote the metal oxide's photoelectrochemical (PEC) performance [88–98]. One such strategy involved the incorporation of reduced graphene oxide into $BiVO_4$ films as doing so helped to create fast, efficient channels for electron transmission [99]. This combination resulted in a rise in the charge separation efficiency and a significant cathode shift of approximately 120 mV in the onset potential of the composite photoanodes. Additionally, Lee *et al.* [92] reported that PO_4-doped $BiVO_4$ in which the phosphate molecule partially replaced V in the monoclinic lattice of $BiVO_4$ showed superior PEC activity. Simply doping with 0.5% phosphate resulted in a 30-fold increase in performance when compared to the bare sample.

Several studies have reported on the use of co-catalysts with $BiVO_4$ photoanodes, in particular electrocatalysts, to improve interfacial reaction activity [95–97]. Choi *et al.* [100] proposed a novel method for the preparation of nanoporous $BiVO_4$ photoanodes (Figure 5) in which the $BiVO_4$ films were further modified with two different layers of co-catalysts, namely FeOOH and NiOOH. The morphology of the nanoporous structure significantly promoted charge carrier separation, resulting in 90% separation at 1.23 V vs. RHE. Loading two-layered co-catalysts in series effectively promoted charge injection by reducing the occurrence of interfacial charge recombination at the interface between $BiVO_4$ and OEC (oxygen evolution catalyst). This technique was also useful for constructing a favorable potential drop at the interface between OEC and the electrolyte. To reduce the risk of overpotential in the $BiVO_4$ photoanodes during water oxidation, Zou *et al.* [97] loaded composite AgO_x/NiO_x electrocatalysts onto the surface of the $BiVO_4$ photoanodes. It was determined that the presence of a composite electrocatalyst stabilized the high valence state of Ag and Ni ions in the two components and the high valence metal ions generated were favorable for creating very active catalytic reaction sites. This not only improved the kinetics of water oxidation, but also created a Schottky junction between the electrode and the electrolyte, thus promoting bulk charge separation.

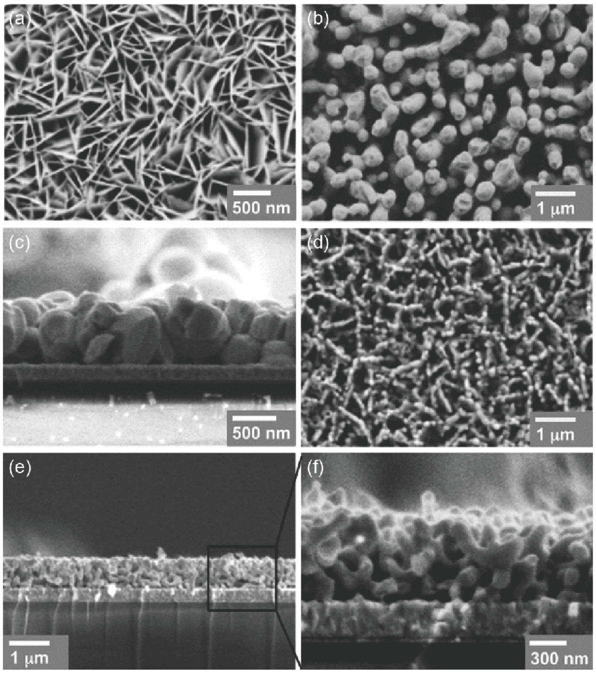

Figure 5 (a) Morphologies of BiOI films, (b) top-view, and (c) side-view SEM images of $BiVO_4$ films prepared using NH_4OH/V_2O_5. (d) Top-view and (e) side-view SEM images of $BiVO_4$ films prepared using DMSO/VO$(acac)_2$, and (f) magnified image of the side view of $BiVO_4$ films. Reprinted from Ref. [95] with permission. Copyright (2014) AAAS.

In making $BiVO_4$ photoanodes that were appropriate for practical photocatalytic applications, extensive research into their photochemical stability was systematically conducted. In several studies, placing a protective layer or using a catalyst layer were common approaches used for inhibiting the onset of corrosion and maintaining the photoanode's stability [101,102]. Other methods were also investigated in detail, including the one reported by Domen *et al.* [103] in which a high-temperature treatment was successfully applied in an effort to improve charge separation and enhance the stability of Mo-doped $BiVO_4$ photoelectrodes. At the same time, the Ni layer was deposited between the Sn layer and the $BiVO_4$ granule film, which transformed it into an electrical back contact and ion source for the catalyst regenerated *in situ*. When the catalytic activity of NiFe-OEC decreased due to material losses, the Ni layer provided a way for the selective replenishment of the NiFe catalyst on the photoanode's surface. Choi *et al.* [102] reported on the occurrence of photocorrosion of $BiVO_4$ photoanodes, and proposed the use of a V^{5+}-saturated electrolyte that would inhibit the dissolution of V^{5+} from $BiVO_4$ lattices, thereby suppressing the photocorrosion process and improving the photochemical stability of $BiVO_4$. The improved $BiVO_4$/FeOOH/NiOOH photoanode maintained a stable photocurrent for 450 h at 0.6 V vs. RHE. $BiVO_4$-based photoanodes were also reported to be photocatalytic materials most suitable for generating hydrogen from seawater. Zou *et al.* [104] used a Mo-doped $BiVO_4$ photoanode that had been modified with RhO_2 to split natural seawater, and based on these results, constructed a photocatalytic seawater splitting system.

2.4 $CuWO_4$

$CuWO_4$ is a visible-light absorbing n-type semiconductor with a band gap above 2.3 eV. Even though it has enjoyed the spotlight as a good photocatalyst, its efficiency at PEC water-splitting reactions were found to be lacking due to poor charge separation and hole collection properties [105–108]. To this end, many innovative methods have been applied to improve the PEC performance of $CuWO_4$.

Researchers found that synthesizing a hybrid structure with a charge transport mediator was an ideal way to improve the performance of $CuWO_4$ [105–107,109,110]. A study conducted by Gaillard *et al.* [109] detailed how films were prepared via spray pyrolysis using a combination of the light-absorbing $CuWO_4$ with electron-transporting multi-wall carbon nanotubes. The composite photoanode effectively reduced bulk resistance by 30% when compared to a pure $CuWO_4$ sample. Also, heterostructure processing was determined to be another effective way of improving the photoanode's water-splitting performance. Herring *et al.* [110] synthesized porous $BiVO_4/CuWO_4$ heterojunction electrodes by spraying $BiVO_4$ onto the surface of the electrodeposited $CuWO_4$ films. The bilayer electrodes had higher photocurrent densities than any individual material, which was attributed to facilitation of the charge carrier collection by the formation of a $BiVO_4/CuWO_4$ heterojunction.

Surface modifiers have also been tested as possible means of improving the PEC performance of $CuWO_4$ photoanodes. As reported by Dunn *et al.* [111], the incorporation of Ag nanowires into a $CuWO_4$ film photoanode via a modified sol-gel method resulted in a current density that was 4-fold higher at 1.23 V when compared to the normal hydrogen electrode (NHE at pH 9) and the bare $CuWO_4$ control sample. Smith *et al.* [112] prepared functionalized $CuWO_4$ photoanodes with TiO_2-coated Au plasmonic nanoparticles attached to the film's surface. The Au plasmonic nanoparticles improved the surface catalytic activity of the electrodes. Additionally, the plasmonic effect promoted the transport of extra charge carriers within the space-charge layer, thereby avoiding the charge recombination process and mitigating the limitations of the $CuWO_4$ photoanodes. Slabon and co-workers [113] used $CuWO_4$ photoanodes modified with Ag_2NCN to gain favorable band-edge positions in $CuWO_4$ and Ag_2NCN which allowed for more efficient charge separation and better PEC performance.

$CuW_{1-x}Mo_xO_4$, which is the solid product of $CuWO_4$ and $CuMoO_4$, was shown to further narrow the band gap under experimental conditions. With a band gap between 2.0 and 2.3 eV, $CuW_{1-x}Mo_xO_4$ allowed for expanded visible-light absorption. Choi *et al.* [114] prepared $CuW_{1-x}Mo_xO_4$ photoanodes via an electrochemical deposition method to determine the parameters needed for optimal PEC water-splitting performance through both experimental operations and theoretical calculations. Li *et al.* [115] generated $CuW_{1-x}Mo_xO_4$ photoanodes via facile spray pyrolysis, and was able to show that the solar photocurrent density increased to 0.46 mA cm^{-2} at 1.23 V vs. RHE. These results are relatively moderate, thus, unremitting exploration is still required to transform $CuW_{1-x}Mo_xO_4$ into the optimal photocatalyst.

2.5 Metal sulfide

2.5.1 CdS

CdS is a promising photocatalyst widely used for splitting water molecules under visible-light irradiation. However, as with most sulfides, CdS usually suffers from an issue of photocorrosion. To deal with this problem, Grätzel *et al.* [116] used colloidal CdS to split water molecules under visible-light irradiation. During the course of that study, it was established that loading ultrathin RuO_2 onto a CdS photocatalyst suppressed photocorrosion without the need for adding sacrificial agents. In this system, RuO_2 acted as a co-catalyst to promote surface redox reactions. Thus, self-corrosion via electron and charge transport was mitigated. Rapid recombination of photogenerated electrons and holes along the CdS material was another problem encountered by researchers. Since the fabrication of a composite photocatalyst is regarded as a good method for facilitating charge separation and transport, Park *et al.* [117] fabricated hybrid photocatalysts which consisted of CdS and multi-walled carbon nanotubes that had been annealed at 500 °C. The carbon nanotubes led to an improvement in the evolution rate of H_2 when compared with both the untreated and acid-treated samples. Additionally, the results also indicated that loading Pt as a co-catalyst led to much better performance when compared to loading with other metal co-catalysts, such as Ni, Ru, Pd, Au, Ag, and Cu. Resiner *et al.* [118] prepared a hybrid CdS/CdO_x photocatalyst for solar reformation reactions of lignocellulose to H_2 (Figure 6). Despite the moderately successful overall conversion efficiency, the system offered the huge advantage of stability for six days under visible light at room temperature. This method was an inexpensive route toward aqueous proton reduction to H_2 through waste biomass oxidation reactions. Zhou and co-workers [119] synthesized composite photoanodes that were composed of WO_3/CdS nanowire arrays. The CdS outer shell was evenly wrapped around the surface of the WO_3 core, which had been constructed as a favorable coaxial heterojunction. When compared to pure WO_3 or CdS nanowires, the composite core/shell nanowires had better photoelectric sensitivity when exposed to visible light. Simultaneously, the core/shell heterojunction helped to facilitate spatial separation and transfer photoinduced charges, thereby increasing the lifetime and photoelectric sensitivity of the photoanode.

2.5.2 $ZnIn_2S_4$

The ternary sulfide, $ZnIn_2S_4$, is considered to be a good photocatalyst due to its excellent crystallinity and stability properties. To date, $ZnIn_2S_4$ is broadly used for photocatalytic H_2 generation. Li *et al.* [120] synthesized stable $ZnIn_2S_4$ photocatalysts via the hydrothermal method and was able to demonstrate that there was no decline in the anode's photocatalytic properties over the course of an experimental time of 150 h. Zhao and co-workers [121] prepared Cu-doped $ZnIn_2S_4$ photocatalysts and noted that Cu-doping tended to destroy the original structure of the $ZnIn_2S_4$ sample while enhancing its photocatalytic properties.

With the exception of ion doping, $ZnIn_2S_4$-based composite photocatalytic materials were found to promote charge transport and enhance photocatalytic activity. A composite thin-film comprised of In_2S_2 and $ZnIn_2S_4$ was synthesized via an ion-exchange method reported by Ye *et al.* [122]. The composite effectively promoted charge separation, particu-

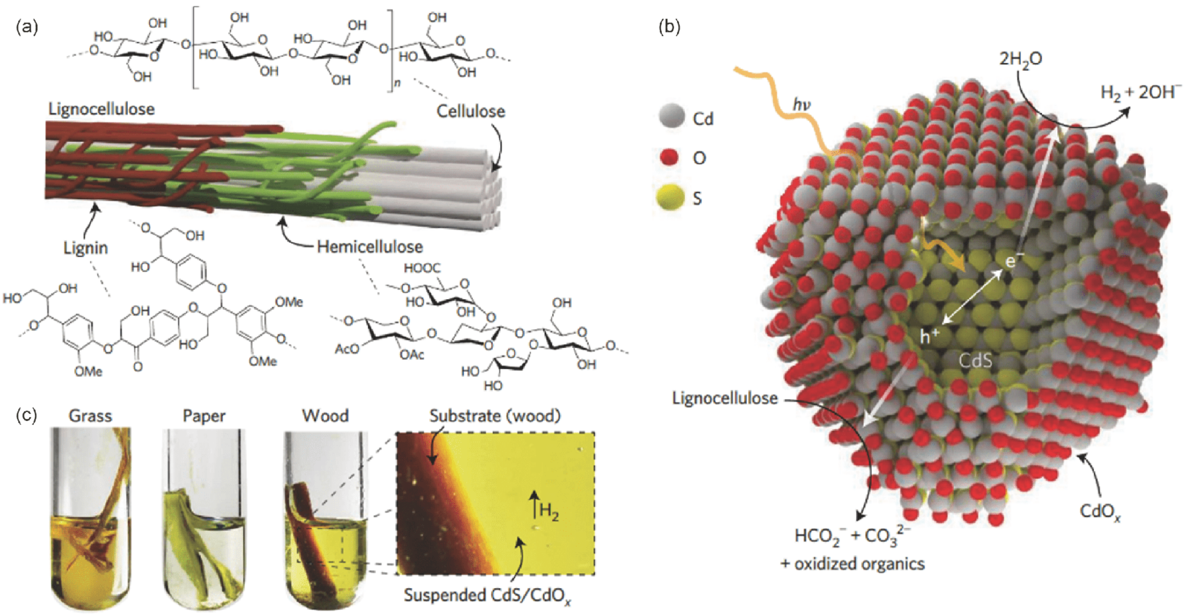

Figure 6 (a) Structural illustration of lignocellulose which is comprised of cellulose surrounded by the less crystalline polymers, hemicellulose and lignin. (b) CdS coated with CdO_x and applied for photoreform reactions of lignocellulose to H_2. (c) As a highly robust photocatalyst, CdS/CdO_x can be used to generate H_2 from crude sources of lignocellulose when suspended in alkaline solution and irradiated with sunlight. Reprinted from Ref. [118] with permission. Copyright (2017) Spring Nature (color online).

larly in cases where the components were evenly distributed, and the composite's interface was smooth. When compared to the individual components of the composite film, the photocatalytic properties of the $In_2S_2/ZnIn_2S_4$ composite showed significant improvement.

Guo *et al.* [123] published details regarding the effects of different transition-metal sulfides, including Ag_2S, SnS, CoS, CuS, NiS, and MnS, on the surface of $ZnIn_2S_4$ photocatalysts that had been loaded with Pt. The results indicated that the dual co-catalyst of Pt and CuS exhibited the best photocatalytic activity among the lot tested. Meng *et al.* [124] applied reduced graphene oxides with good conductivity to light-absorbing $ZnIn_2S_4$ that had been loaded with MoS_2 as the co-catalyst. The simultaneous presence of reduced graphene oxide and MoS_2 effectively promoted quick transport and reaction of the photogenerated electrons, thereby suppressing electron-hole recombination and significantly enhancing H_2 evolution rate of the $ZnIn_2S_4$/RGO/MoS_2 photocatalytic system.

2.5.3 Cu_2ZnSnS_4

Cu_2ZnSnS_4 (CZTS), an abundant multi-component complex sulfide with a band gap of 1.5 eV, showed great promise in photovoltaic and photocatalytic applications [125–127]. However, synthesis of CZTS usually required high temperature and vacuum conditions, which caused excessive production costs and limited further research progress. Various modified approaches have been explored for the preparation of CZTS nanocrystals and films. Gao *et al.* [126] generated CZTS using a low-cost hydrothermal method. In this preparation, a surfactant was not required and the crystal size was controlled using ammonia. The CZTS nanocrystals performed very well during photocatalytic H_2 generation tests in both slurry systems and on thin films. In order to prepare efficient solar-conversion equipment, Zou *et al.* [127] applied a modified solution method to synthesize CZTS films with large grain sizes and vertical penetration structures. The precursor used in the method was aged in air under high humidity for some time before it was used to fabricate the thin films. Improvements in the solution method significantly promoted the growth of CZTS grains and enhanced the solar-driven water-splitting properties of CZTS as thin-film photocathodes.

Other metal sulfides, including ZnS and $AgInS_2$, were considered to be excellent photocatalysts, particularly for photocatalytic splitting of water molecules [128–131]. Many of them were shown to be highly efficient for advanced applications, such as CO_2 reduction, organic synthesis, and N_2 fixation.

2.6 Metal nitrides and oxynitrides

2.6.1 Ta_3N_5

Ta_3N_5 was extensively studied as a photoanode, because it possessed a desirable band gap (2.1 eV) that allowed for the absorption of visible light up to 600 nm. This metal nitride had a suitable band structure straddle for redox potentials of water with a maximum solar-to-hydrogen conversion efficiency of 15.9% [132–137]. Ta_3N_5 was first investigated as a potential photoanodic material by Domen and co-workers [138] in 2004. Ta_3N_5 photoanode films were prepared by a two-step method for conductive substrates. The Ta_3N_5 powders were first synthesized via nitridation of the precursors at high temperatures under ammonia flow. Subsequently, the Ta_3N_5 photoanode films were synthesized by transferring the Ta_3N_5 powders to conductive substrates via the electrophoretic deposition (EPD) method [139–141]. To ensure improved interaction between Ta_3N_5 and the substrate, several reported methods were used for the preparation of Ta_3N_5 photoanodes on Ta foil, including thermal oxidation [138,142], a hydrothermal process [143,144], and electrochemical anodization [20,145]. These were done in order to form a Ta_2O_5 layer on the Ta foil which was subsequently subjected to nitridation to generate Ta_3N_5. The Ta_3N_5 polyhedron array photoanode was fabricated via molten salt-assisted nitridation of the Ta_2O_5 layer on Ta foils so as to obtain a low onset potential for water oxidation [146]. Another way to prepare Ta_3N_5 photoanodes was via the nitridation of $NaTaO_3$ film on Ta foils under ammonia flow [147,148]. Ta_3N_5 photoanodes were also synthesized using a Ta precursor via a carbonate-assisted nitridation method that reduced the need for a preoxidation process for the metal Ta [149]. Synthesis of the Ta_3N_5 photoanodes was achieved via either pulsed laser deposition [150] or atomic layer deposition [151] of Ta_2O_5 films, followed by post-nitridation under ammonia atmosphere. In addition, Ta_3N_5 photoanodes were also synthesized in one-step via atomic layer deposition [152,153] and reactive sputtering methods [154].

2.6.2 *TaON*

TaON has a band gap of 2.5 eV that corresponds to an optical absorption band edge of 500 nm [136]. The valence band and conduction band positions of TaON were ca. 2.2 and −0.3 V vs. NHE at pH 0, respectively, which straddled the redox potential limits of water [137]. TaON photoanodes were synthesized using a two-step method in which the TaON particles were first prepared via nitridation of a Ta_2O_5 precursor under NH_3 before being transferred to a conductive substrate via the doctor blade technique [155] or the EPD method [139,156]. TaON films were also be prepared via thermal nitridation of Ta_2O_5 film grown using the pulsed laser deposition technique [150] or anodization of Ta foils [157]. In addition, TaON films were prepared using the atomic layer deposition method [152]. Abe and co-workers [155] first created porous TaON photoanodes by simply spreading TaON particles on a conductive fluorine-doped tin oxide (FTO) substrate {Higashi, 2012 #22989}. However, the PEC performances of these photoanodes were far below the theoretical value of ca. 6.5 mA/cm^2, even after being subjected to “nicking” treatment using $TiCl_4$ solution; this was attributed to poor electron transport within the photoanodes [157]. Various strategies have been proposed to enhance the PEC performance of TaON photoanodes, including forming highly crystalline TaON particles [158], elemental doping [34,159], nanostructuring [32,157], electrocatalysts [139,160], and manipulating O/N ratio defects [161]. Increasing the temperature of nitridation to obtain high quality TaON crystals greatly improved electron transport and decreased bulk recombination, resulting in better PEC performance [158]. Allam and co-workers [157] reported the preparation of TaON nanorod arrays photoanodes via anodization and nitridation of Ta foils. The optimized 1D morphology enhanced optical properties and increased the ratio of the depletion layer to the photoanode bulk, thus resulting in outstanding PEC water-splitting performance. Deposition of co-catalysts, such as CoO_x and IrO_2, on the TaON photoanodes efficiently promoted charge separation and suppressed self-oxidative deactivation of photoanodes, resulting in better PEC performance [139,160]. By manipulating the nonstoichiometric defects of bulk O/N ratios in TaON photoanodes, Li and co-workers [161] were able to increase both the space-charge layer width and the film’s conductivity, thus resulted an improved performance in water-splitting reactions.

2.6.3 *Perovskite oxynitride*

Perovskite oxynitrides, such as ABO_2N (where A=Ca, Sr, Ba, and B=Nb, Ta), $LaTiO_2N$, $PrTaO_2N$ and $ABON_2$ ($LaNbON_2$, $LaTaON_2$), also have the appropriate band structure for solar-driven water-splitting reactions [162–166]. In several studies, perovskite oxynitrides were synthesized via nitridation of the corresponding oxide or carbonate precursor at high temperatures (between 800 and 1300 °C) under ammonia [163,164,167–170]. To date, only some particle-assembled oxynitride films, which were prepared via the transfer of oxynitride powders to conductive substrates using electrophoretic deposition or particle transfer methods, have been investigated for PEC water-splitting purposes [170–173]. However, poor charge carrier transport properties were seen between the film particles themselves and between the film particles and the conductive substrate; this led to serious electron-hole recombination issues [174]. The exposed region of the underlying conductive substrate caused losses in reaction efficiency due to back reduction of the photo-oxidized intermediates [174,175]. Various efforts were made to improve their PEC performances, including employing highly crystalline $LaTiO_2N$ particles with reduced grain boundary densities and using a plateau solar photocurrent for solar-driven water splitting of 6.5 mA/cm^2 [172]. The interparticle charge transport observed on $SrTaO_2N$ films was ameliorated by H_2 annealing as the lower oxygen concentrations on the surface improved both electrical conductivity and charge separation efficiency [173]. The electron-hole recombination in particle-assembled oxynitride films were reduced by controlling bulk defects and interface engineering. Thus, the photocurrent value for $LaTaON_2$ photoanodes was 2.1 mA/cm^2 at 1.6 V vs. RHE, which was achieved by increasing bulk electrical conductivity and reducing back reactions on the conductive substrates [176]. Deposition of the Co-Pi/Al_2O_3 layer on a $CaNbO_2N$ photoanode greatly enhanced PEC performance due to the Co-Pi co-catalyst's ability to improve the kinetics of oxygen evolution and the reduced occurrence of recombination on the Al_2O_3 surface layer [177].

3 Carbon nitride polymers for photocatalysis

The main issue with using PCN for photocatalysis is the solar-conversion efficiency, which is still incomparable with the efficiency of inorganic materials [14]. In polymers, it was found that the photoexciton formed displayed strong Coulomb forces, ultimately leading to easier electron and "hole" recombination. Meanwhile, the low degree of polymerization resulted in insufficient charge migration [178]. In a recent review, several studies reported attempts to improve the performance of PCN photocatalysis through optimization of molecular composition, the structures present on the photoanode, crystallinity, using a hybrid system, and via co-catalysts for photoredox reactions, all of which will be discussed in this section [15,179–187].

3.1 Molecular engineering of PCN

Thermal condensation is a facile, widely adopted method for the polymerization of triazine and heptazine tectons into conjugated systems. Nitrogen-abundant organic molecules, such as cyanamide, dicyanamide, and both triazine and heptazine derivatives, were used as precursors [188,189]. The amorphous or semi-crystalline melon-based PCN material produced, which is usually referred as "bulk CN", "graphitic-C_3N_4" or "g-C_3N_4", was comprised of one-dimensional (1D) heptazine (tri-*s*-triazine) units linked by bridging imide units via zigzag-type chains, as shown in Figure 7. These chains were connected via hydrogen bonds which then shape them into a two-dimensional (2D) arrangement that was distinct from the form predicted for graphitic-C_3N_4 [181]. Incomplete polymerization of the precursor resulted in the formation of amorphous or semi-crystalline phases with a large number of non-condensed surface amino groups.

Initial research into melon-based PCN showed only moderate activities for photocatalytic water-splitting reactions [190]. One reason for this was the low conductivity of the disordered structure, which ultimately induced insufficient charge separation and transfer along the polymer.

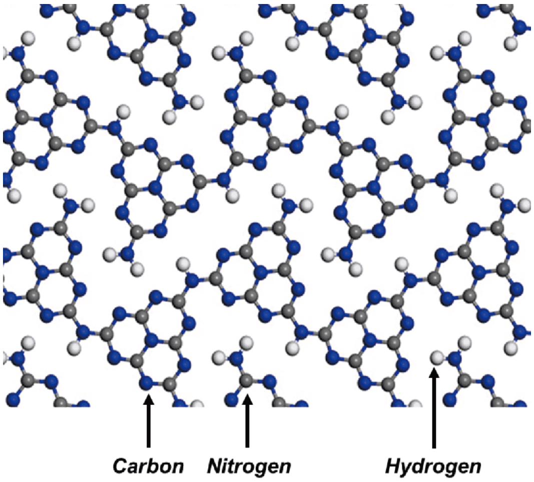

Figure 7 Illustration of melon-based PCN photocatalysis (color online).

Also, it was reported that pristine PCN was only able to absorb at the lower end of the spectrum (460 nm), which is only a snippet of the entire solar spectrum [191]. For this reason, many strategies were developed to improve its performance, specifically those aimed at enhancing the activities of PCN through doping with heteroatoms [192], copolymerization [193,194], the use of nanostructures [195], crystallizing [196], sensitization with dyes [197], delamination to a few layers thickness [198], and coupling with other semiconductors or conductors. In addition, PCN that was synthesized as thin films was capable of splitting water by applying voltage bias, as this significantly improved separation of the excitons. Oxygen and hydrogen evolution processes in the experiments were physically separated, thus allowing for the collection of pure oxygen and hydrogen gases without the need for any membrane barrier.

Incorporation of heteroatoms or homo-atoms into the PCN matrix extended electron delocalization and improved its solar-conversion efficiency. A typical example is the modification of PCN via copolymerization of urea and 1,3,5-cyclohexanetriol [199]. Diverse coplanar graphited carbon rings were introduced into PCN's conjugated network at various depths from the surface. The gradual rearrangement of band levels and the subsequent built-in electric field dramatically promoted charge-pair separation and transfer. The PCN catalyst that had been modified via gradual doping exhibited a photocatalytic H_2 evolution rate of 230.6 μmol/h under λ>420 nm irradiation which was 21 times higher than that of pristine PCN [199].

Recently, a PCN-based donor-acceptor (D-A) system was used to simulate photosystem II. In detail, a selenium and cyanamide-functionalized heptazine-based melon was prepared via thermal condensation of trichloromelamine and potassium selenocyanate, and later employed as a D-A light harvester [200]. Combining the photosystem and the electron shuttle into a single species, both of which displayed n- and p-type semiconducting properties, enhanced the light-harvesting ability of the system. This endowed DA-HM with greater efficiency in the separation and transfer of photo-excited charge carriers, leading to improved photocatalytic activity for H_2 evolution [200].

Moreover, controlling the quantity of nitrogen or carbon in the PCN framework helped to influence the occurrence of defects and enhance the photocatalytic activity of PCN under visible excitation; this was on account of narrower band gaps and increased surface activity present in the system [201]. Nitrogen defects were introduced into PCN via the addition of an alkali compound (e.g., KOH) during thermal polymerization of melamine, urea or thiourea. The g-C_3N_x products that were obtained possessed tunable band structures controlled by the cyano groups located in the bulk and surface N vacancies. They were able to capture visible light and separate photoexcited charge carriers more efficiently than pristine PCN. The g-C_3N_x-0.01 sample afforded a H_2 evolution rate of ca. 69 μmol/h which was twice that of pristine PCN [201]. Thus, this alkali-assisted route enabled facile synthesis of PCN with tailored optical and photocatalytic properties.

Carbon vacancies in the PCN matrix could be controlled through a constant-temperature steam-etching approach. Such defects functioned as active sites for CO_2 activation since the COOH* intermediate species could be stabilized (Figure 8). Meanwhile, the lifetime of the photogenerated charges were prolongated, thus enhancing the solar efficiency for CO_2 to CO conversions. To further promote the efficiency of PCN photocatalysts, both 2,4,6-triaminopyrimidine (TAP) condensation with thiourea and steam engineering were employed to synthesize PCN-TAP-CVs. The PCN-TAP-CVs photocatalyst that was obtained showed a 45-fold improvement in CO_2-to-CO conversion activity over pristine PCN. The apparent quantum yield (AQY) of the PCN-TAP-CVs was 4.8 % at 420 nm [202].

Recently, a new type of triazine-based PCN was prepared using a photochemical method [203]. The band gap of the PCN was 1.7 eV, which was remarkably narrower than that of typical PCN semiconductors (ca. 460 nm). With this system, most of the visible spectrum could be absorbed during the oxidation of alcohols and the reduction of CO_2. This represented a vital step toward advancing the development of red-light-responsive triazine-based structures for solar applications [203]. This type of material has attracted significant scientific interest since it could be used to extensively harvest visible light and inspire more advanced real-world application of the technology.

3.2 Structural engineering of PCN

Another approach for the development of better PCNs was to control the micro/nanostructure of the polymers. Mesoporous structures significantly increased the number of active sites when compared to their pristine counterparts due to their improved charge-transfer capabilities. Of late, a variety of methods have emerged for the preparation of nanoporous PCNs, namely the hard-template approach and the use of a self-assembly method. Vinu and co-workers [204] synthesized mesoporous carbon nitrides with a C_3N_5 stoichiometry by condensing 3-amino-1,2,4-triazole using KIT-6 silica template in a nano-casting approach. The mesoporous PCN possessed a 3D porous and graphitic structure with a tri-*s*-triazine framework, and its surface was connected via triazole units [204]. Mesoporous PCN material with a band gap of ca 2.2 eV had a superior photocatalytic H_2 evolution rate of 267 μmol/h under visible-light irradiation, a result which was much higher than that seen for bulk PCN [204].

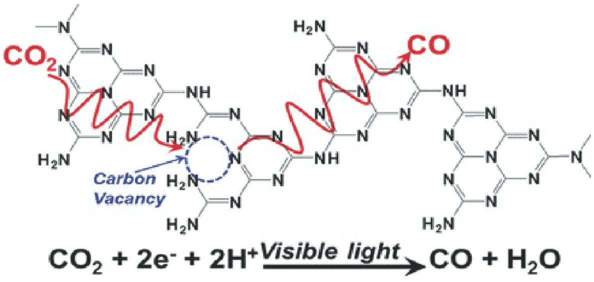

Figure 8 Formation of a carbon vacancy via steam etching. Reproduced with permission from Ref. [202]. Copyright (2019) Wiley-VCH (color online).

In addition to the hard-template method, a facile self-assembly method was developed to produce self-supported PCN aerogels without using any template or cross-linking agents (Figure 9) [205]. Incorporating a larger surface area into functional groups and the 3D network structure endowed these freestanding PCN aerogels with excellent photocatalytic properties for H_2 evolution and H_2O_2 production under visible-light irradiation. These results meant that utilizing hard-template and self-assembly strategies to construct PCNs with 3D structures held great promise for solar-to-chemical energy conversion applications [205].

Since the structure of a bulky PCN material was similar to that of graphite which had been assembled with multiple layers of the melon, peeling the bulky structure into its individual single or few-layered nanosheets was also of scientific interest as there was great potential for the unique optoelectronic properties which emerged as a result, namely the presence of surficial active sites and shortening of the diffusion paths for carriers. To date, a variety of delamination methods have been developed, including sonication exfoliation, protonation exfoliation, ball-milling, and thermal etching. Additionally, organic reagents or strong acids were used for the exfoliation processes.

In a more environmentally friendly approach, few-layered PCN nanosheets were synthesized via steam reformation.

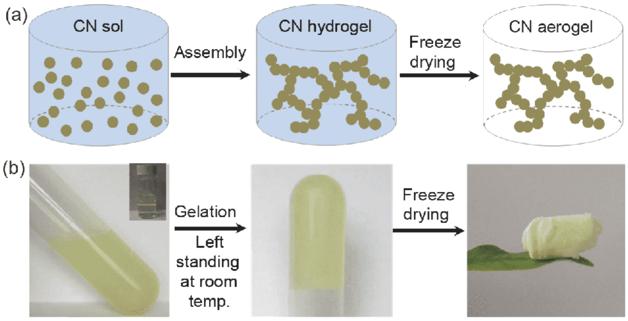

Figure 9 (a) Synthesis of the PCN aerogel. (b) Photographs of colloidal solutions of PCN nanoparticles (inset: tyndall effect of PCN nanoparticle in aqueous solution), PCN hydrogels, and PCN aerogels. Reproduced with permission from Ref. [205]. Copyright (2017) Wiley-VCH (color online).

Using urea as the precursor, bulk PCN-U was effectively peeled into few-layered nanosheets via steam reformation processes. The thicknesses of the PCN-U nanosheets and the bulk PCN-U were approximately 1.2 and 3.5 nm, respectively [206], which was clear evidence of this method's effectiveness (Figure 10). The lifetime of the photogenerated charges was significantly prolonged using this delamination strategy (from 57.01 ns for bulk PCN-U to 301.25 ns for PCN-U nanosheets), and the separation efficiency of the photogenerated charges was also improved. Impressively, the PCN-U nanosheets (without any extra doping/modification) exhibited robust photocatalytic activity for H_2 production under visible-light irradiation, with an AQY of 11.3% at 405 nm [206].

In addition to a top-down synthesis route, Fu *et al.* [207] developed a conventional bottom-up method for preparing porous few-layer PCNs. This approach involved the use of a molecular self-assembly to form layered precursors, alcohol molecules intercalation, and subsequent thermal induced exfoliation and polycondensation. The few-layered PCN exposed more active sites for the separation of charge carriers, thus it exhibited superior photocatalytic activity and was very stable for photocatalytic H_2 production and oxidative coupling reactions of benzylic amines to form imines under visible-light irradiation [207].

Redox organo-synthesis reactions were also attempted using structured PCN photocatalysts. For example, the construction of layered PCN polymers based on tri-*s*-triazine units was achieved using nucleobases (adenine, guanine, cytosine, thymine, and uracil) and urea to build a 2D semiconducting structure which allowed for a variety of band-gap engineering applications [208]. Using these PCN polymers yielded energized charge carriers with light irradiation. This induced photoredox reactions for redox transformations of organic molecules that consisted of amines and alcohols, as well as the coupling of C–C, C–O, C–N and N–N bonds [208].

In addition to its 2D layered structure, construction of PCN films on a conductive substrate had important practical applications for solar-driven redox reactions in PEC systems. The doctor blade technique was used as a general pathway for synthesizing highly porous PCN films with controllable chemical and photophysical properties on a variety of substrates [208]. A supramolecular paste was prepared by mixing 1.29 g cyanuric acid, 1.26 g melamine, and a small amount of barbituric acid in water (denoted here as CMBA$_x$, where x=0, 0.05, 0.1, and 0.15 refers to the mass of barbituric acid in the supramolecular precursor). The growth of PCN films, which were ascribed to the formation of the supramolecular paste, contained monomers in ethylene glycol that could be casted onto different substrates (Figure 11). The composition, porosity, and optical properties of PCN were fine-tuned by controlling the design of the supramolecular paste, which led to a continuous porous PCN network upon calcination [208]. The strength of the porous structure was demonstrated through its high electrochemically active surface area, remarkable dye adsorption, and its PEC and photodegradation properties. The simplicity, scalability, and controllability of the final PCN composition open new opportunities for its use in photocatalysis, electronics, and energy-related applications.

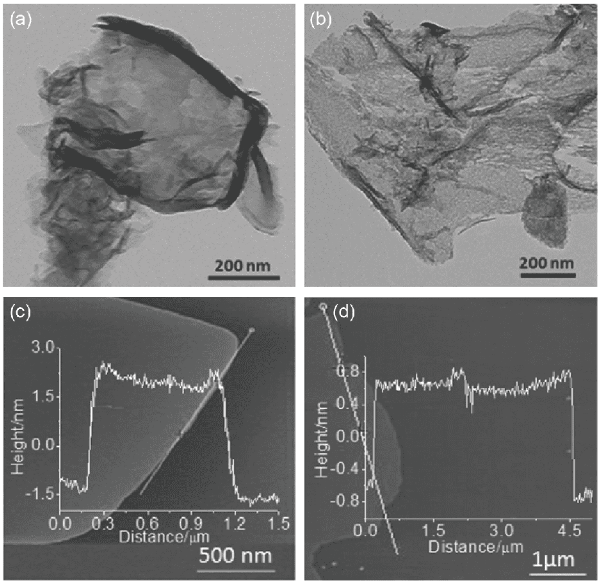

Figure 10 Transmission electron microscopy (TEM) images of (a) bulk PCN-U and (b) PCN-U nanosheets. Atomic force microscopy images of (c) bulk PCN-U (inset is the height image) and (d) PCN-U nanosheets (inset is the height image). Reproduced with permission from Ref. [206]. Copyright (2017) Wiley-VCH.

Wang *et al.* [209] reported synthesizing PCN films on FTO substrates using various precursors. Photoactive films were synthesized through a conventional molten-mediate polymerization method. More importantly, it has found that the films were only formed when the precursor was mixed with a sulfur-containing compound and a non-sulfur compound. As a result, a photocurrent density value of ca. 100 μA/cm^2 at

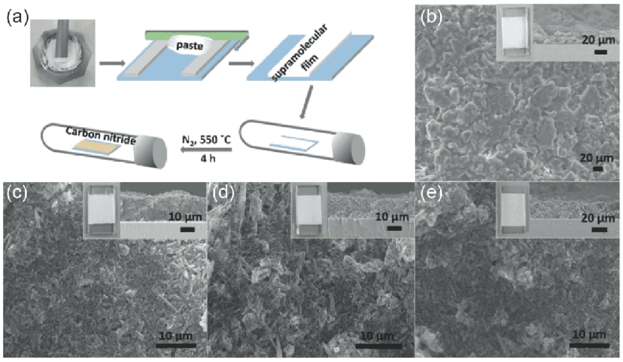

Figure 11 (a) Illustration of the doctor blade preparation method, (b–e) scanning electron microscope images of supramolecular precursors films prepared from (b) $CMBA_{(0)}$, (c) $CMBA_{(0.05)}$, (d) $CMBA_{(0.1)}$, and (e) $CMBA_{(0.15)}$. The cross-sectional scanning electron microscope images of the corresponding films are shown in the inset. Reproduced with permission from Ref. [208]. Copyright (2018) Wiley-VCH (color online).

1.23 eV vs. RHE was observed. This was attributed to the presence of S, which enhanced adhesion between the FTO and PCN films. When these PCN films were phosphorylated via treatment with H_3PO_4 solution, the photoconversion efficiency further rose to 120 μA/cm^2 at 1.23 eV vs. RHE due to the increased valence band anchoring the phosphates onto the surface of the PCN film [210]. Tang and co-workers [211] reported doping PCN films with a controlled precursor made from a mixture of dicyandiamide (DCDA) and boric acid. These boron-doped PCN films were formed through rapid thermal condensation. It was determined that the boron content in these films gradually seeped from the bottom to the top of the films. This resulted in increased charge separation and transfer with an enhanced photocurrent density of ca. 103.2 μA/cm^2 at 1.23 eV vs. RHE.

PCN films were also formed on conductive Y-doped ZnO nanorods as photoanodes for solar-driven water-splitting reactions [212]. A single rod of the photoanode is shown in Figure 12. In this scenario, the weakness of the charge separation and transfer was compensated for by using conductive nanorods. The resulting photocurrent density was 0.4 mA/cm^2 at 1.23 eV vs. RHE. In addition, the optoelectronic properties of the photoanode were comprehensively investigated [212].

3.3 Crystalline carbon nitride polymer

Crystalline carbon nitride (CCN) formed with the same heptazine unit as the melon-based photoanode displayed different optoelectronic properties. Theoretically, CCN's high crystallinity resulted in a narrower band gap, enhanced light-harvesting efficiency, and an increase in the minor charge diffusion length due to its extended π-conjugated system and delocalized π-electrons. Therefore, the quantum efficiency of these systems was significantly improved.

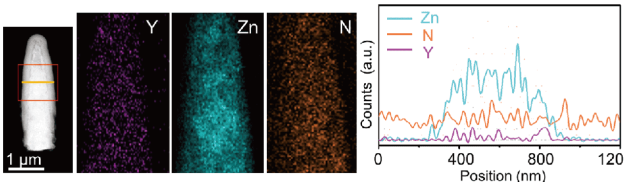

Figure 12 The scanning transmission electron microscopy of single 0.8% Y:ZnO@PCN core-shell nanorod. Reproduced with permission from Ref. [212]. Copyright (2018) Wiley-VCH (color online).

An ionothermal/molten-salt method is the typical route for the synthesis of CCNs. Bojdys and co-workers [213] used LiCl-KCl as an eutectic mixture in a high-temperature solution to mediate the course of polymerization and obtain a CCN polymer. This ionothermal method was adopted for the synthesis of a triazine-based CCN with a poly(triazine imide) (PTI) structure and high crystallinity. Recently, surface kinetic controls were utilized to achieve solar-driven overall water splitting via crystalline PTI frameworks [214]. Loading Pt as a co-catalyst on the PTI surface played a crucial role in inducing overall water-splitting reactions. Co-deposition of the cobalt species effectively increased the photocatalytic activity and adjusted the ratio of H_2 and O_2 produced during the reaction while enhancing the stability of the photocatalyst itself. Optimal samples with the dual co-catalysts had an AQY of 2.1% for the entire water-splitting reaction [214].

In addition to the photoanode's crystalline properties, the type of subunit in the CCN polymer was another major factor contributing to its photocatalytic activity. Compared to triazine-based PTIs, this tri-*s*-triazine-based CCN was expected to be a more promising photocatalyst due to its improved charge mobility. In this context, tri-*s*-triazine-based CCN was synthesized using preheated melamine as a starting material in combination with the molten-salt method [196]. The resulting sample exhibited high photocatalytic activities for H_2 and O_2 production from the water-splitting process [196]. By adding phosphate to mimic natural photosynthetic circumstances, the AQY for H_2 production was 50.7% at 405 nm.

Moreover, the influence of various temperatures on the photocatalytic activities of heptazine-based CCN prepared using this ionothermal approach was investigated [215]. CCN synthesized using a precursor pre-heated to 550 °C exhibited the highest photocatalytic activity for H_2 evolution; an AQY of 6.8% at 420 nm was observed with methanol as the sacrificial agent. In comparison with the previously referenced P25, CCN_{550} showed remarkable photocatalytic H_2 production under visible-light irradiation while P25 remained inactive. The amount of hydrogen gas produced by CCN_{550} was close to P25 under full arc irradiation of Xe lamp, which highlighted the potential of this type of crystalline conjugated polymer for the future development [215].

Taking advantage of a top-down strategy, tri-*s*-triazine-based CCN nanosheets (CCNNS) were extracted from its bulk counterparts via a sonication-centrifugation process [198]. CCNNS possessed a well-defined, unambiguous structure with minimal thickness, large aspect ratios, homogeneous tri-*s*-triazine-based units, and high crystallinity. CCNNS showed significantly enhanced photocatalytic H_2 generation activity under visible light when compared to PCN, PTI, and bulk tri-*s*-triazine-based CCNs. A high AQY of 8.57% at 420 nm for H_2 production from an aqueous methanol feedstock was achieved using tri-*s*-triazine-based CCNNS. The inherent structure of its 2D crystals inferred ultrathin tri-*s*-triazine-based CCNNS many advantages that could have potentially far-reaching effects in applications relating to bioimaging as well as energy storage and conversion projects [198].

Furthermore, the combined strategy of ionothermal and copolymerization as a synthetic route was used to customize the electronic band structure and texture of CCNs. Copolymerization of urea and oxamide followed by post-calcination in molten salt resulted in a highly crystalline species with heptazine-based maximum-layer stacking units at a distance of 0.292 nm (Figure 13) [216]. By taking advantage of the reduced interlayer stacking distance and the extended spectral absorption, more photons dissociated, and the reactive surface charges increased, as reflected by a dramatic rise in the H_2 evolution activity under visible-light conditions, peculiarly in the spectral region above 500 nm. The AQY values for H_2 evolution of these optimized samples were 57% and 10% at 420 and 525 nm, respectively, thus, highlighting the usefulness of synergistic optimization between the crystal structure and D-A copolymerization in order to significantly promote exciton dissociation and hot charge carrier yields.

CCNs with poly-heptazine-imide (PHI) structures were synthesized via one-pot polymerization of a stable monomer with a high nitrogen content (5-aminotetrazole) in the presence of a salt mixture (NaCl/KCl); this functioned as a way to modulate the photocatalyst's crystallinity, grain boundary structure, and general chemistry [217]. Diverse salts (NaCl/KCl or LiCl/KCl) were used to modify the formation of local packing, crystallinity, and grain boundaries (Figure 14). A well-constructed PHI structure enhanced optical absorption and optimized electronic properties, thus contributing outstanding photocatalytic performance. The AQY value for H_2 production was 65% at 420±1.0 nm and was achieved in the presence of K_2HPO_4 as a double layer modifier [217]. In addition, PHI-based carbon nitrides were also found to be highly active photocatalysts in CO_2 reduction reactions as well as during Rhodamine B and 4-chlorophenol degradation under visible light [218]. These studies provided insight into the use of carbon nitrides with well-ordered PHI structures for enhanced solar energy transformation applications.

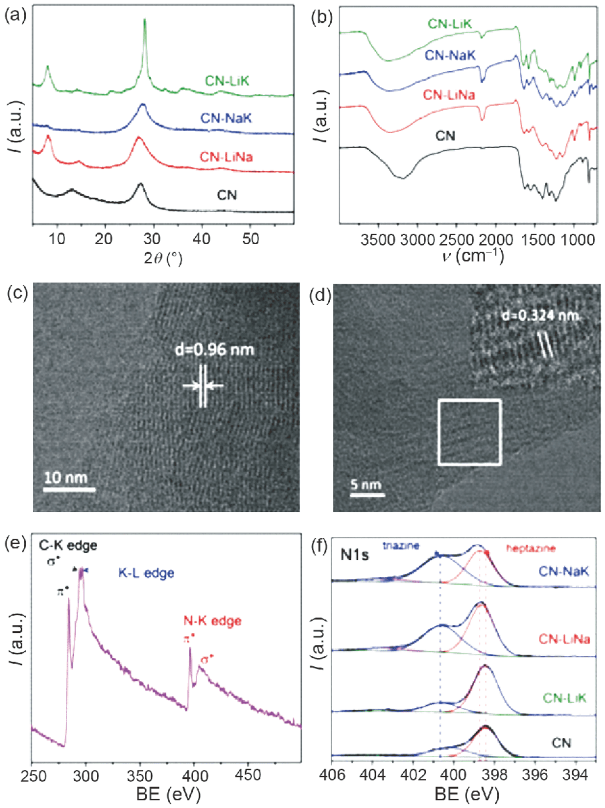

Figure 13 (a) Powder X-Ray diffraction patterns and (b) Fourier transform infrared spectra of CN, CN-LiNa, CN-LiK, and CN-NaK; (c, d) TEM images of CN-NaK (inset: enlargement of the selected area); (e) electron energy loss spectrum of CN-NaK; (f) N 1s high-resolution XPS spectra of CN, CN-LiNa, CN-LiK, and CN-NaK polymers. Reproduced with permission from Ref. [216]. Copyright (2017) Wiley-VCH (color online).

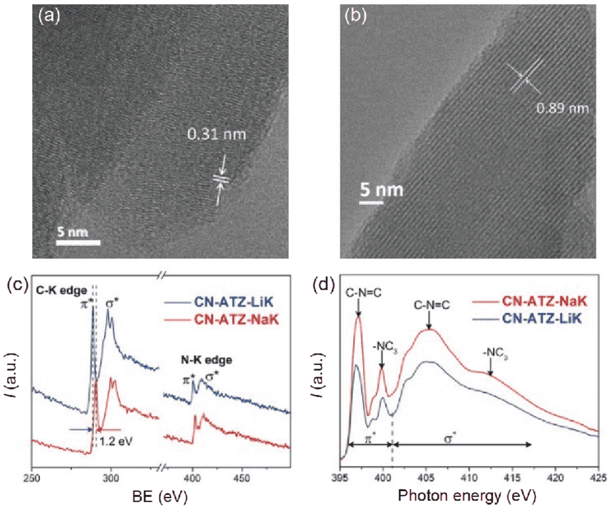

Figure 14 (a, b) TEM images of CN-ATZ-NaK; (c) electron energy loss spectra, and (d) N-K edge X-ray absorption near edge structure analysis results of CN-ATZ-LiK and CN-ATZ-NaK samples. Reproduced with permission from Ref. [217]. Copyright (2019) Wiley-VCH (color online).

Additionally, the construction of triazine-heptazine D-A heterostructures promoted interfacial charge transfer and enhanced photocatalytic activity [216]. A triazine-heptazine copolymer was synthesized via simple post-calcination of PCN in NaCl/KCl eutectic salts in an effort to regulate the polymerization process and optimize the structure of the photocatalyst. The inherent triazine-heptazine D-A heterostructure dramatically accelerated interface charge transfer and boosted the photocatalytic activity (AQY value was 60% at 420 nm). This study demonstrated the importance of intermolecular D-A copolymers in NaCl/KCl molten salts with higher melting points in regulating the chemical structure and properties of the CN matrix, especially for cases where there was an absence of lithium.

Crystal studies were also performed during the PEC water-splitting reaction. Via thermal condensation, Shalom *et al.* [219] attempted to construct films using CCN powder in which closely packed CCN films were achieved via crystallization of the CN monomers on a conductive substrate. A photocurrent density of ca. 116 μA/cm^2 at 1.23 eV vs. RHE was obtained, which was much higher than the thin films synthesized using the general melon powder. However, note that it was still difficult to synthesize these films via an *in situ* approach since the presence of the molten salt damaged the conductive substrate. Thus, an alternative synthetic approach is necessary for improving the crystallinity of PCN films.

3.4 Hybrid PCN photocatalyst

Integrating PCN with other semiconductors was typically employed when using traditional metal oxides such as $BiPO_4$ [220], CdS [221], and many others [179]. Despite the improved reaction efficiency of this approach, its mechanistic pathway remains unclear. Recent developments have shown that the hybrid system could be used for other challenging applications with enhanced solar-conversion efficiency, including solar-driven water-splitting reactions and N_2 fixation. A series of hybrid systems was created using organic semiconductors such as polypyrrole, graphitized polyacrylonitrile, poly(3-hexylthiophene), poly(3,4-ethylenedioxythiophene), and polyfluorene. More interestingly, carbon quantum dots (CQDs) that had been implanted in the surface plane of the PCN nanotubes were synthesized via thermal polymerization of freeze-dried urea and CQD precursors [222]. The CQD-implanted PCN nanotubes (CCTs) simultaneously improved visible-light absorption capabilities, facilitated photoelectron transport, and suppressed charge recombination through their specifically coupled heterogeneous interface. CCTs showed efficient photocatalytic performance in H_2 evolution and a marked AQY of 10.94% at 420 nm [222]. Rational combination of CQDs with PCN was shown to lead enhanced photocatalytic performance in H_2 evolution. Also, it was revealed that PCN could be processed into quantum dots for photocatalysis. For instance, integration with mesoporous TiO_2-SiO_2 (Me-TSCN) significantly increased the specific surface area via carbon nitride quantum dots, resulting in favorable adsorption of the reactant molecules and increased mass transfer of the reaction products [223].

In one study, PCN was used to capture visible light and activate Co^{2+} sites in a photochemical CO_2-to-CO conversion reaction without the need for additional ligands [224]. Photocatalysts containing single Co^{2+} sites on PCN were prepared using a deposition approach. Under visible-light irradiation, these photocatalysts demonstrated prominent activity with a turnover number of more than 200 and high selectivity toward CO formation. Given the unique structure of PCN, its framework N atoms were able to coordinate with and activate Co^{2+} sites for selective CO_2 to CO reduction reactions [224].

In another study, an alternative approach via the formation of a Z-scheme system composed of two photocatalysts was proposed [225]. In this scenario, one photocatalyst, namely OEP (oxygen evolution photocatalyst), had a low valence edge and, thus, was suitable for photocatalytic oxygen evolution. The other photocatalyst, namely hydrogen evolution photocatalyst (HEP), possessed a high conduction edge that was capable of evolving hydrogen. Under illumination, OEP and HEP facilitated oxygen and hydrogen evolution, respectively. The photoexcited electrons from OEP were neutralized with the "holes" from the HEP via bridging using conductors such as pure metal, doped metal oxides, or conductive carbon [226]. This was also achievable by directly binding two photocatalysts that displayed low mismatch of their crystalline structures. For PCN systems, reduced graphene oxide (RGO) nanosheets served as a solid electron mediator linking Fe_2O_3 nanoparticles with PCN nanosheets via chemical bonding and π-π stacking of the electric field. The emerging Fe_2O_3/RGO/PCN ternary heterojunction displayed improved photocatalytic efficiency during water-splitting reactions (Figure 15). RGO nanosheets were capable of accelerating interface charge transfers between PCN and Fe_2O_3, as evidenced by the enhanced photocurrent and fluorescence quenching abilities. The crucial role of RGO was also seen in other PCN-based Z-systems ($BiVO_4$/RGO/PCN and WO_3/RGO/PCN), illustrating the versality of this strategy. All in all, this study provided a new perspective on the construction of solid-state Z-scheme systems using RGO as an electron mediator. This, in turn, provided insight into the construction of other solid-state systems [225].

To extend the range of potential redox applications, other photocatalytic reactions using hybrid PCN materials were also investigated. PCN was shown to undergo coupling with metal nanoparticles, inorganic semiconductors, and metal-ligand complexes during photocatalytic CO_2 reduction. Thus, a hierarchical direct heterojunction system was proposed that was composed of urchin-like hematite (α-Fe_2O_3) and PCN. This photocatalytic system showed improved

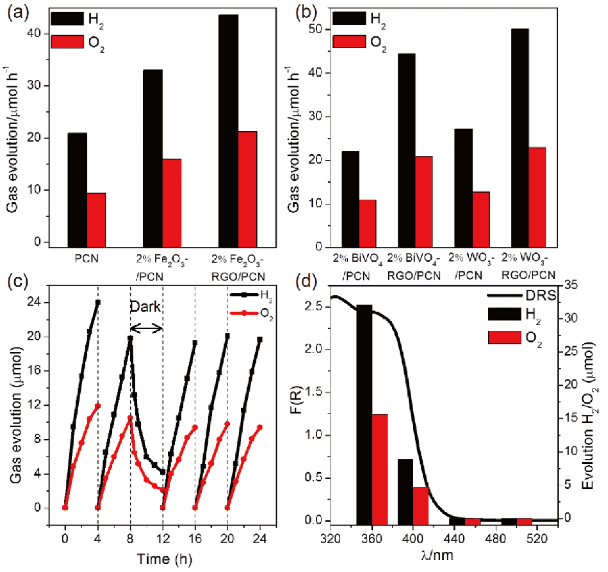

Figure 15 (a) Photocatalytic overall water-splitting activity of PCN, Fe_2O_3/PCN, and Fe_2O_3/RGO/PCN under full arc irradiation from a Xenon light source. (b) Photocatalytic overall water-splitting activity of WO_3, WO_3/reduced graphene oxide (RGO), $BiVO_4$, and $BiVO_4$/RGO-modified PCN under full arc irradiation. (c) Overall water-splitting activity of Fe_2O_3/RGO/PCN under visible-light irradiation (>400 nm). (d) Wavelength dependence of the rate of water-splitting for Fe_2O_3/RGO/PCN. Reproduced with permission from Ref. [225]. Copyright (2019) Wiley-VCH (color online).

photocatalytic activity for CO_2-to-CO reduction reactions [225]. In one study, the 3D hierarchical structure of the urchin-like hematite and its superior fundamental sites facilitated CO_2 adsorption, and the unique Z-scheme feature was shown to efficiently promote the separation of electron-hole pairs as well as strengthen the reducibility of electrons in PCN's conduction band [227]. For photo-driven CO_2 fixation reactions, more efficient and selective photo-stimulated CO_2 reduction was noted in the presence of an iron-complex catalyst and a mesoporous carbon nitride (mpg-CN). As a result, irradiation in the visible region ($\lambda \geq 400$ nm) of a CH_3CN/triethanolamine (4:1, *v*/*v*) solution containing $[Fe(qpy)(H_2O)_2]^{2+}$ (qpy=2,2′:6′,2″:6″,2″-quaterpyridine) and mpg-CN led to CO evolution with 97% selectivity, a turnover number of 155, and an AQY of ca. 4.2% [227].

In another study, metal-free black phosphorus (BP) nanosheets were impregnated to create PCN nanosheet (BP/CNS) photocatalysts [228]. The BP/CNS showed exceptional performance in both visible-light nitrogen photofixation and pollutant reduction reactions due to the increased number of excited electrons present and the improved efficiency of separation for the charge carriers which was achieved via the formation of C–P covalent bonds. Furthermore, the optimal BP content in BP/CNS's chemical structure remained unchanged even after exposure to air for 30 days or after five cycles of photocatalytic nitrogen fixation. This was because the lone electron pairs on the phosphorus atoms largely boosted BP's chemical stability [228]. There is still the challenge of determining if the ammonia was obtained by photocatalytic conversion as well as establishing the extent of conversion in the presence of a N-abundant photocatalyst, since N was so easily released in the matrix due to strong photo-incidence.

3.5 Co-catalysts for PCN photocatalysis

In one study, surface kinetic control was presented as a viable pathway for creating active sites and reducing the over-potential during water cleavage reactions. Loading specific co-catalysts onto PCN provided an efficient, facile, and cost-effective strategy for the evolution of hydrogen [229] and oxygen [230], water-splitting processes, CO_2 reduction, and other practical redox reactions [231]. Specifically, co-catalysts offered sites for trapping photogenerated charges and promoted charge separation kinetic on the surface. Even though Pt has been widely utilized as a co-catalyst with PCN for photocatalytic H_2 evolution reactions, replacing the noble metal was shown to be useful for many practical applications.

Transition-metal-based co-catalysts are of great interest in the scientific community due to the nature of their active sites, surface structural arrangements, and structure-activity relations [232]. In one study, a catalyst system powered by visible-light was developed for efficient H_2 evolution by depositing nickel phosphide (Ni_2P) as a co-catalyst onto PCN [232]. Without using any noble metal, the system showed comparable catalytic activity with Pt-loaded CN. This was attributed to effective electron-hole separation, as well as migration and transfer processes in the excited state which made Ni_2P/PCN an efficient photocatalyst for proton reduction. More importantly, surface reaction was significantly improved when compared with that seen in PCN photocatalysis [232].

Another study reported a rational structural design for photocatalysts with uniform and isolated active sites in an effort to promote charge separation and proton reduction reactions, both of which were central to improving photocatalytic efficiency [233]. Catalysts that were dispersed on an atomic level provided insight into reaction kinetics of the active site, especially when these catalysts were comprised of mononuclear metal complexes or single metal atoms. Photocatalysts consisting of intimately anchored single atoms on semiconductors were shown to significantly boost charge separation through the promotion of chemical bonding. A single-site-based photocatalyst containing Co sites dispersed on an atomic level securely anchored PCN for extremely efficient solar-driven hydrogen evolution. Co was trapped via the adoption of the Co_1-N_4 geometry as an active center for activating H−H bond formation processes, thus leading to more efficient H_2 evolution. The transition-metal single-site photocatalysts generated in this study were shown to be low-cost, high performance catalysts with far-reaching implications for real-world applications. The reaction design presented in this study exploited the efficacy of these single-site catalysts by extending their coupling networks to include various isolated metal complexes and other framework supports [233].

In terms of the evolution of H_2 during a redox processes, water oxidation reactions are considered more difficult since PCN displays weak oxidation ability when it encounters the barrier created by O–O band formation. In one study, a sustainable and effective water oxidation system was developed using PCN and cubic cobalt manganese spinel (c-$CoMn_2O_4$) as light transducer and water oxidation co-catalyst, respectively [234]. The surface of PCN was modified with c-$CoMn_2O_4$ which served to quicken the interface transfer rate of the charge carriers and reduce the excessive energy barrier encountered during O–O formation. This, in turn, resulted in enhanced photocatalytic activity for water oxidation. The well-designed surface of PCN-$CoMn_2O_4$ (CN-CM) composites showed enhanced photocatalytic performance during water oxidation reactions. The OER of CN-CM was four times higher than that of pristine PCN, while an AQY value of ca. 1% at 380 nm was noted with $AgNO_3$ as the sacrificial agent [234]. New insights into the design and progress of efficient PCN-based photocatalysts for water oxidation were garnered from this study.

Direct pure water-splitting processes were achieved through rational synthesis of an appropriate PCN matrix and modification using suitable co-catalysts. A facile method was developed to specifically load Pt and Co_3O_4 nanoparticles onto the interior and exterior surfaces of hollow carbon nitride spheres (HCNS) in order to promote the surface redox functions of the polymer semiconductors under investigation [235]. The photocatalytic water-splitting activities of HCNS with spatially separated oxidation and reduction centers at their nanodomains were reinforced through these interactions. Improved activity was attributed to the presence of spatially divided reactive sites for H_2 and O_2 evolution and also via the unidirectional migration of the electron and hole pairs on the Janus surface, thereby preventing the occurrence of unwanted reverse reactions of the water-splitting process and decreasing charge recombination [235].

In addition to solar-driven water-splitting reactions, the use of co-catalysts is of importance in increasingly complicated reactions. For instance, Cu species were introduced into PCN for photocatalytic anaerobic methane conversion to ethanol [236]. Cu-modified PCN influenced the generation and *in situ* decomposition of H_2O_2 to produce ·OH. Additionally, the Cu species possessed active sites for methane adsorption and activation. When combined, these features helped to reduce the number of redundant ·OH radicals present during overoxidation and facilitate methane conversion. A hypothetic mechanism for a methane-methanol-ethanol pathway was proposed, in which the synergy between the Cu species and the adjacent C atom in PCN for C_2 product was highlighted [236].

A mussel-inspired strategy was developed to yield silver-impregnated ultrathin PCN nanosheets. By using Ag as the co-catalyst on optimized PCN nanosheets, remarkable performances were then noted for organic degradation and H_2O_2 production (Figure 16). Owing to the valence band holes which had been photogenerated and the selective two-electron reduction of O_2 via conduction of the band electrons, an efficient, economic, and environmentally friendly route for light-driven H_2O_2 production was established with an initial rate of 0.75×10^{-6} m/min. The modified photocatalytic performance was primarily attributed to the large surface area of the ultrathin PCN nanosheet layer, the surface plasmon resonance effects induced by Ag nanoparticles, and the cooperative electronic capture interactions that existed between Ag and ultrathin PCN nanosheets. Accordingly, this unique photocatalyst was found in the extended absorption region of the spectrum, which effectively inhibited the recombination of electron-hole pairs and promoted electron transfer in photocatalytic reactions [237].

4 Mechanistic insights into key surface processes in semiconductor photocatalysis

In all the studies that we reviewed, what made semiconductor photocatalysis particularly interesting was the method by which reactions were initiated. Unlike thermal catalysis, the reductive and oxidative half reactions in semiconductor photocatalysis were initiated by photogenerated electrons and holes with equal equivalents respectively. In most cases, the reductive and oxidative half reactions were stably isolated and occurred on different

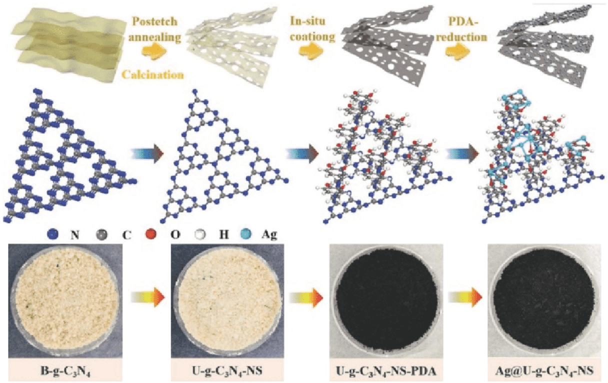

Figure 16 Stepwise representation of the route to Ag nanoparticles impregnated with ultrathin PCN nanosheets (last column) and homologous molecular structures as well as photographs of the corresponding resultants for each step. Reproduced with permission from Ref. [237]. Copyright (2019) Wiley-VCH (color online).

surface sites of the semiconductor catalysts. For instance, on TiO_2 catalysts, electrons that were excited to the conduction band (e_{cb}^-) were trapped in surface Ti sites, whereas the remaining valance band holes (h_{vb}^+) were immobilized in surface O sites. For catalysts containing numerous exposed facets, the distinct energetic levels of the various facets were the driving force behind the reductive and oxidative reactions [238]. However, this did not mean that the two half reactions were independent of each other; in fact, it was shown that the opposite situation held true. For instance, since O_2 was the most widely employed e_{cb}^- scavenger in semiconductor photocatalysis, the reduction of O_2 by e_{cb}^- was used to determine the rate of the oxidation reaction triggered by h_{vb}^+, as the recombination reaction between e_{cb}^- and h_{vb}^+ was found to be influenced by the accumulation of e_{cb}^-. In addition, the reduction of O_2 by e_{cb}^- was not simply a direct multi-electron reduction to water. It was established that sequential single-electron reduction generated reactive oxygen species (ROS) like $O_2^{\cdot-}$, H_2O_2 and ·OH, which also served as major participants in oxidative reactions. In the photocatalytic organic transformations, namely the selective oxidation of alcohols, amines, and alkanes mediated by TiO_2, the transfer of O atoms from O_2 to the corresponding products was dominant, thus, a concerted effort was exhibited by both h_{vb}^+ and e_{cb}^- of TiO_2 in the creation of the oxidation products [13,239].

Another connection between the reductive and oxidative half reactions was the proton transfer process. Since stoichiometry of photocatalytic reactions often included the simultaneous gain or loss of electrons and protons, proton transfer processes played a critical role in balancing the charges of each half reaction. In one study, the participation of proton transfer processes in the redox reactions strongly affected electron structures and local charges in the transition state, thus exerting influence on the energetic profile and reaction pathway. The occurrence of proton-coupled electron transfer (PCET) processes in which electrons and protons were simultaneously transferred meant that the formation of high-energy intermediates was avoided and reaction efficiency was increased [240–242].

The aim of this section is to summarize the recently developed mechanistic approaches to two elementary reactions in semiconductor photocatalysis: O_2 reduction and water oxidation. Particular focus is placed on two aspects, namely: (1) the activation of O_2 and its direct participation in oxidative reactions; and (2) proton transfer processes on the surface of metal oxide catalysts and their effects on the interfacial redox steps.

4.1 O_2 activation in semiconductor photocatalysis

O_2 is the most frequently used electron scavenger in photocatalytic reactions. Studies have shown that the efficient capture of e_{cb}^- by O_2 prolonged the lifetime of h_{vb}^+, which was the major driving force behind oxidative reactions such as pollutant degradation or organic transformations. On the other hand, the reduction of O_2 to water by e_{cb}^- occurred via a multi-step process with a total transfer of $4e^-$ and $4H^+$. The ROS generated during this complex process, such as $O_2^{\cdot-}$, H_2O_2 and ·OH, were strongly oxidative and participated in oxidative half reactions. Additionally, molecular O_2 formed adducts with the intermediate radicals produced via h_{vb}^+ oxidation, thus triggering further oxidation processes. Since the pathways for O_2 participation in oxidative reaction were varied and numerous, product distributions and reaction efficiency were significantly affected.

Generally, on the surface of a TiO_2 catalyst, the reduction of O_2 proceeded via a sequential single-electron transfer with the formation of various ROS (Eqs. (1)–(5)). Among these ROS, the relatively stable H_2O_2 accumulated in considerable amounts during TiO_2-based photocatalysis and, thus, were utilized for *in situ* synthesis of low concentrations of H_2O_2. Additional one-electron reduction of H_2O_2 then generated ·OH, one of the major oxidative species in photocatalytic oxidation. However, this pathway toward ·OH generation via O_2/H_2O_2 reduction has been long overlooked since the water oxidation initiated by h_{vb}^+ (Eq. (6)) was regarded as the primary source of ·OH.

$$O_2 + e_{cb}^- \rightarrow O_2^{\cdot-} \tag{1}$$

$$H^+ + O_2^{\cdot-} \rightarrow HO_2^{\cdot} \tag{2}$$

$$2HO_2^{\cdot} \rightarrow H_2O_2 + O_2 \tag{3}$$

$$HO_2^{\cdot} + e_{cb}^- + H^+ \rightarrow H_2O_2 \tag{4}$$

$$H_2O_2 + e_{cb}^- \rightarrow \cdot OH + OH^- \tag{5}$$

$$H_2O + h_{vb}^+ \rightarrow \cdot OH + H^+ \tag{6}$$

In one study, the degradation of aromatic pollutants was initiated through hydroxylation of phenyl rings [243], which was the prerequisite for ring-opening and further mineralization [244]. Hydroxylation mainly proceeded via an attack of the phenyl ring by ·OH derived from either water oxidation (Eq. (6)) or the multi-step O_2 reduction reactions (Eqs. (1)–(5)). Owing to the relatively high yield at the primary stage of the degradation reaction and the ease with which the hydroxylated products were detected using LC-MS or fluorescence spectroscopy [245], the hydroxylation of aromatics was a good model for investigating the ·OH generation pathway. Labeling the O atoms in water and O_2 using ^{18}O and ^{16}O isotopes, respectively, allowed researchers to trace the source of the O atom in the ·OH that was generated in the reaction (Eq. (7)). Based on this process, Matsumura *et al.* [244] were able to show that O_2 made significant contributions to the hydroxylation of benzene. The contribution ratio was largely dependent on the phase of the TiO_2 present;

in anatase, typically between 10% to 30% of the O atoms in the generated phenol were obtained from O_2, whereas the ratio in rutile remarkably increased to between 60% and 80%. Although a detailed pathway for the incorporation of the O atom during hydroxylation was not revealed in this work, such a high O_2 contribution ratio during hydroxylation, especially in the presence of rutile TiO_2, prompted the need to reexamine of the direct role of O_2 in photooxidative degradation as research into this field has long been overlooked, in particular, when compared to research focused on "direct hole" oxidations on the catalyst's surface.

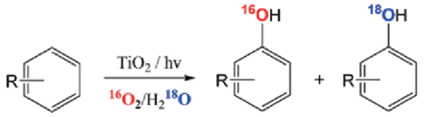

(7)

For an in-depth approach on the mechanism by which O_2 was incorporated during photocatalytic hydroxylation, Li and co-workers [246] selected benzene and benzoic acid with different adsorption capabilities on TiO_2 catalysts as model substrates. The aim of this study was to establish which contributions were made during surface and bulk reactions. In the photocatalytic oxidation system containing benzoic acid and benzene coexisting within the same dispersion, the percentage of O_2-derived hydroxyl O atoms in the hydroxylated products of strongly adsorbed benzoic acid (ca. 30%) was much less than that seen in the case of weakly adsorbed benzene (>60%). This difference in the abundance of the isotopes was attributed to the different contributions made by the surface and bulk reactions. For the surface reactions, the holes directly oxidized the aromatics undergoing hydrolysis to generate the respective hydroxylated products; thus, the O atoms in hydroxyl group mainly originated from water. In contrast, the oxidation source in the bulk reactions was •OH and $O_2^{\bullet-}$, both which contributed to water oxidation and O_2 reduction alike. From this, it was concluded that bulk oxidation was dominant for weakly adsorbed substrates, whereas more O atoms from O_2 molecules were integrated into the hydroxyl group of the oxidation products.

Although it was well accepted that the multi-step reduction of O_2 generated ·OH, most of the earlier experiments indicated that ·OH from the reduction of *in situ* H_2O_2 did not exert significant effects on the photooxidation of organic substrates. Instead, experimental observations pointed to the theory that the O atoms from O_2 were incorporated into the hydroxylated aromatics via a Russel-like pathway ($R\cdot + O_2 \rightarrow ROO\cdot$) [247–249] typically applied during the oxidation of aliphatic substrates. In this pathway, adducts of the superoxide radical $O_2^{\cdot-}$ on the phenyl ring were regarded as major intermediates toward the incorporation of O atoms into hydroxylated aromatics. However, Li and co-workers [243] found that the addition of superoxide dismutase (SOD), which disproportionated $O_2^{\bullet-}$ to O_2 and H_2O_2, exerted very little impact on the O_2 contributions to the hydroxyl O atoms in the hydroxylated products. However, when the ·OH quencher, isopropanol, was added to the reaction, O_2 decreased from 26.6% to 18.6%. This meant that ·OH played a more pivotal role in the incorporation of oxygen atom into hydroxylated aromatics than its $O_2^{\bullet-}$ counterpart. Moreover, since peroxidase (POD) was known to quench H_2O_2 generated *in situ*, its presence in the reaction led to a dramatic decline to 4.9% for the ratio of the O atoms in the hydroxyl groups obtained from O_2. Altogether, the external addition of H_2O_2 led to the incorporation of the O atoms in H_2O_2 into the hydroxyl group, thus, it can be concluded that the *in situ* formation of the intermediate H_2O_2 played an essential role in the O_2 incorporation process. The ·OH generated from the reduction of H_2O_2 was the final active species through which O_2-derived O atoms were introduced into the hydroxylated product. Further investigation revealed that h_{vb}^+ was not the only active species that initiated oxidation during the photocatalytic reactions. Even in the absence of h_{vb}^+, the substrate was still oxidized by the ·OH formed from the reduction of O_2 by e_{cb}^- [185]. Therefore, the importance of this pathway for photocatalytic oxidations cannot be neglected as its contribution is on par with that of h_{vb}^+.

In one study, it was shown that O_2 played a more significant role in the extended ring-opening of aromatics during the follow-up step after hydroxylation. The aromatic rings were cleavage as a prerequisite of poly-hydroxylation. Mono- or di-carboxylic acid products were the primary ring-opening products (Figure 17(A)) [250], but the true source of oxygen in the final acid products remains unclear. To determine the ring-opening mechanism and the pathway for O_2 insertion, 3,5-di-tert-butylcatechol (DTBC) was employed as a model substrate due to the relatively high yield (between 25% and 30%) of ring-opening products at the primary stage of degradation [251]. For photocatalytic degradation on a TiO_2-based catalyst, primary degradation products from the three proposed reaction pathways were identified via GC-MS [251], as shown in Figure 17(B). Products **2**–**5** were ring-opening products, of which, **2** and **3** were intradiol products containing an O atom inserted into the middle of the ortho-hydroxyl, **4** and **5** were extradiol products with an O atom inserted into the two outer hydroxyl groups, and **6**–**8** were auto-oxidation products of DTBC without cleavage of the C–C bond. The yield obtained for the intradiol products was 7 to 10 times higher than that of the extradiol products, and was indicative of a dominant intra-inserting pathway during the ring-opening process. The origin of the inserted O atoms in the ring-opening product was traced using isotope labeled $H_2{}^{16}O/{}^{18}O_2$ or $H_2{}^{18}O/{}^{16}O_2$. It was established that for the highest yielding product, **2**, most of its O atoms (>98%) originated from O_2, whereas the ratio of O atoms from O_2 for

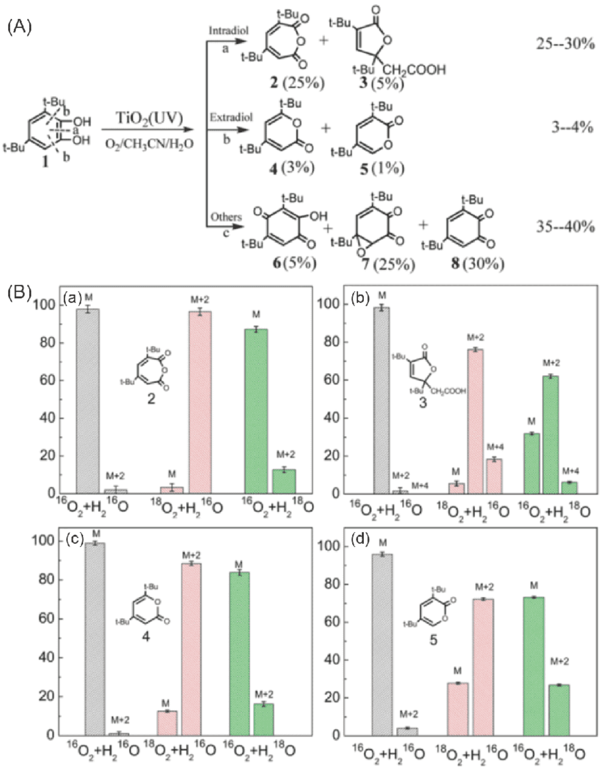

Figure 17 (A) The three pathways and their respective products of the primary degradation of DTBC. (B) *O*-isotope distribution of the four primary ring-opening products under various isotope conditions, M, M^{2+}, and M^{4+} denote products that include 0, 1, and 2 atoms, respectively, of substituted ^{18}O in place of ^{16}O. Reproduced with permission from Ref. [251]. Copyright (2014) American Chemical Society (color online).

products **4** and **5** was a little smaller than 85% and 75%, respectively. This discrepancy was due to the occurrence of reversible hydrolysis and subsequent O-exchange interactions with water. This extremely high O_2 contribution also exceeded the upper limit for the ratio of ·OH derived from O_2 [243,244]. Therefore, it was concluded that cleavage of the sp^2 C–C bond in an aromatic compound was not via a traditional out-sphere oxidation through h_{vb}^+ or ·OH. Instead, molecular O_2 was responsible for severing the C–C bond and inserting an O atom.

Pang's work [251] looked at the effect of the coordination unsaturation of surface Ti sites on the distribution of intradiol and extradiol products. It was found that the intradiol/extradiol ratio exhibited a positive linear correlation with the size of the TiO_2 particles, and that the increase in the number of surface defects favored the extradiol product. They proposed that the reaction sites of four-coordinated Ti_{4c}, which were mainly located at the step or edge of the TiO_2 crystal (Figure 18(b)), were needed for the formation of intradiol products, whereas the low-yielding extradiol products were delivered from the corners with the smallest distribution proportion on the catalyst's surface by three-coordinated Ti_{3c} or Ti sites associated with the oxygen vacancies. Activation of O_2 was performed by Ti^{3+} due to the availability of a Ti site for O_2 coordination (Figure 18(c)). Except for these two, most of the surface sites on the terraces that were unable to form a five-membered ring complex with DTBC exhibited very little activity and were products of either auto-oxidation or some other unknown oxidation process (Figure 18(a)). Based on these findings, a relationship between the O_2 activation pathway and specific surface sites was established.

Given that O_2 activation exerted substantial effects on the efficiency of aerobic photocatalytic reactions, possible ways for improving the efficiency of O_2 activation or even deliberately switching the O_2 activation pathway warranted in-depth exploration. The multi-step reduction of O_2 to H_2O_2, ·OH or H_2O was an electron-transfer system, and the stoichiometry associated with these photocatalytic reactions involved simultaneous gain or loss of protons. Despite the fact that most research has been focused on the electron-transfer processes in O_2 reduction, the effects of proton transfer remain largely overlooked because the concurrent transfer of electrons and protons in redox reductions, referred to as PCET, was avoided altogether through the formation of local charge-accumulated intermediates with a high-energy barrier. Given that both the energetics and the reaction pathway were greatly influenced by the sequence in which electrons and protons were transferred, the role and mechanism of the PCET process in homogeneous catalytic systems was thoroughly investigated [240–242]. However, unlike the results obtained in homogeneous systems in which the energetics of the electron donor and acceptor were localized and the sites for the proton donor and acceptor were quite specific at molecular and atomic level, electrons in heterogeneous photocatalysis were transferred between the delocalized bands of photocatalyst and the localized states of the adsorbed molecules and the protons were transferred within the complex hydrogen bond network associated with the water adsorbed onto the surface.

In Mayer's work [252], the presence of protons exerted significant effects on the photocatalytic redox abilities of colloidal ZnO nanoparticles in aprotic toluene/THF solution. With Cp^*_2Co (Cp*=pentamethylcyclopentadienyl) as the electron donor, it was established that 1 to 3 electrons were stored in each ZnO particle, whereas its electron storage capabilities were noticeably enhanced in the presence of protonic acid to over 15 electrons per nanoparticle. Also, the protons in this scenario neutralized excessive accumulation of negative charges. Moreover, the existence of a concerted proton and electron-transfer process on either colloidal ZnO or TiO_2 catalysts during heterogeneous photocatalysis was demonstrated for the first time [253]. The single-electron reduction reaction of TEMPO (2,2,6,6-tetramethyl-piperidin-1-yl-oxyl) or *t*Bu_3ArO· (2,4,6-tri-tert-butylphenoxyl radical) to their corresponding anions ($TEMPO^-$ or *t*-Bu_3ArO^-) was thermodynamically unfavorable via out-sphere electron-transfer processes in non-polar solvents. Colloidal ZnO and

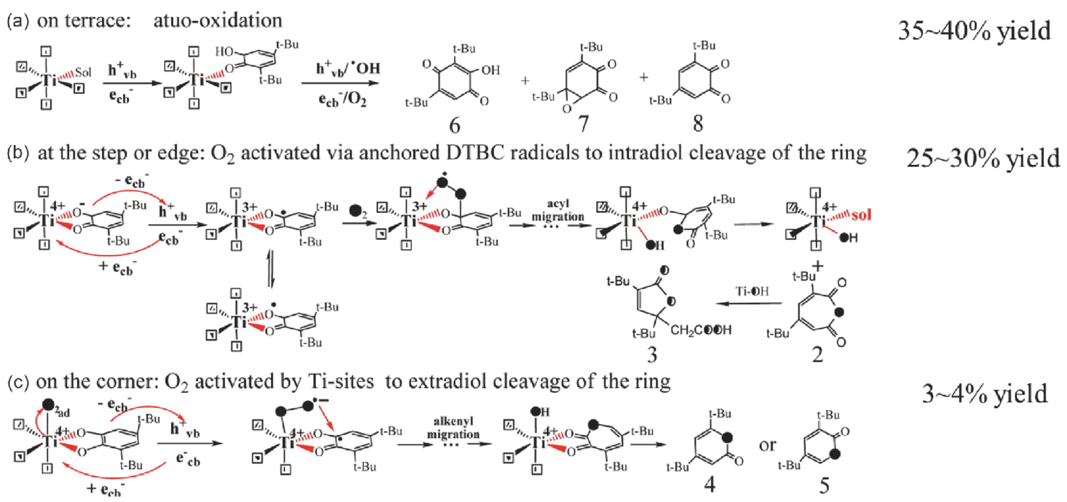

Figure 18 Proposed mechanism for individually incorporated O atoms during the photocatalytic cleavage of DTBC by TiO_2. (a) Auto-oxidation via ·OH/h_{vb}^+ on terrace, (b) intradiol cleavage via the anchored DTBC radicals for active dioxygen at the step or edge, (c) extradiol cleavage via Ti-site active O_2 on the corner of the interface. Reproduced with permission from Ref [251]. Copyright (2014) American Chemical Society (color online).

TiO_2 nanoparticles capped with organic ligands like dodecylamine or oleic acid were illuminated upon UV light irradiation in aprotic toluene. Electrons accumulated on these particles at the expense of oxidation of the organic ligands or organic residues. Protons were also released during sacrificial oxidation of these organics, and subsequently adsorbed onto the surface of the particles in an effort to balance the negative charges present. Subsequent addition of TEMPO or *t*-Bu_3ArO· to air-free toluene solutions containing ZnO/e^- or TiO_2/e^- yielded re-oxidized particles and their corresponding reduction products, TEMPOH or *t*Bu_3ArOH. These products were too thermodynamically unfavorable to originate via out-sphere electron-transfer processes; instead, they were the result of a concerted electron and proton transfer.

The aforementioned results demonstrated how reduced metal oxides were capable of transferring both electrons and protons, a concept which expanded our current understanding of interfacial redox reactions. When taken into consideration along with the insights previously gained on the role of H^+/e^- coupling on TiO_2 and ZnO in photocatalytic, electrocatalytic or photoelectron-catalytic systems, it became clear why PCET was a common theme for proton-related interfacial redox reactions on metal oxide catalysts. In the other words, proton-related redox reactions such as the previously discussed O_2 reduction, were significantly affected by proton transfer processes. This provided a unique strategy for adjusting surficial O_2 reduction mechanistic pathways by controlling the associated proton transfer processes.

Inspired by these findings, Sheng *et al.* [254] used phosphate in a select model reaction since it was known to strongly adsorb to TiO_2 surfaces and modulate both the proton concentrations and the photodegradation of aromatics. Indeed, the presence of phosphate was shown to significantly enhance photocatalytic degradation of aromatics. More intriguingly, the accumulation of H_2O_2 in the reaction system was suppressed to only 1/40 of the concentration on pristine TiO_2, and further reduction of H_2O_2 to H_2O was noticeably depressed due to blockage of the required reaction sites by adsorbed phosphate. Electrochemical tests also demonstrated that the Faraday efficiency of O_2 reduction to H_2O_2 at a bias of −0.5 V vs. NHE was only 0.6% on phosphate-modified TiO_2 when compared to the 31% observed on pristine TiO_2 (Figure 19(A)). Rotating disc electrode tests demonstrated that the addition of phosphate switched the O_2 reduction on TiO_2 from a sequential single-electron transfer process to a direct $4H^+/4e^-$ reduction to H_2O, thus avoiding H_2O_2 generation altogether [254]. Moreover, it was found that not all anions with buffer properties exerted similar influence over the O_2 reduction pathway. Polyprotic acids like L-glutamic acid and malonic acid behaved in the same manner as phosphate (Figure 19 (A)), in that binding to TiO_2 facilitated multi-electron/proton transfer processes and bypassed the generation of H_2O_2. However, monocarboxylic acids like acetic acid and propionic acid exerted little effect on the reaction pathway in spite of their ability to enhance the overall rate of O_2 reduction.

It was proposed that, after anchoring on the TiO_2 surface with one of its acid groups, polyprotic acid used another of its acid group as a proton relay pendant to increase the local proton concentration and facilitate proton transfer to the reaction center through an oriented hydrogen bond network during O_2 reduction (Figure 19(B), Scheme (a)) [254]. In this regard, more efficient PCET processes were achieved when proton transfer increased, directing O_2 reduction to a one-step, concerted $4H^+/4e^-$ pathway. In contrast, surface-adsorbed monocarboxylic acids lacked the pendant acid/base group needed for such a reduction pathway, as the only

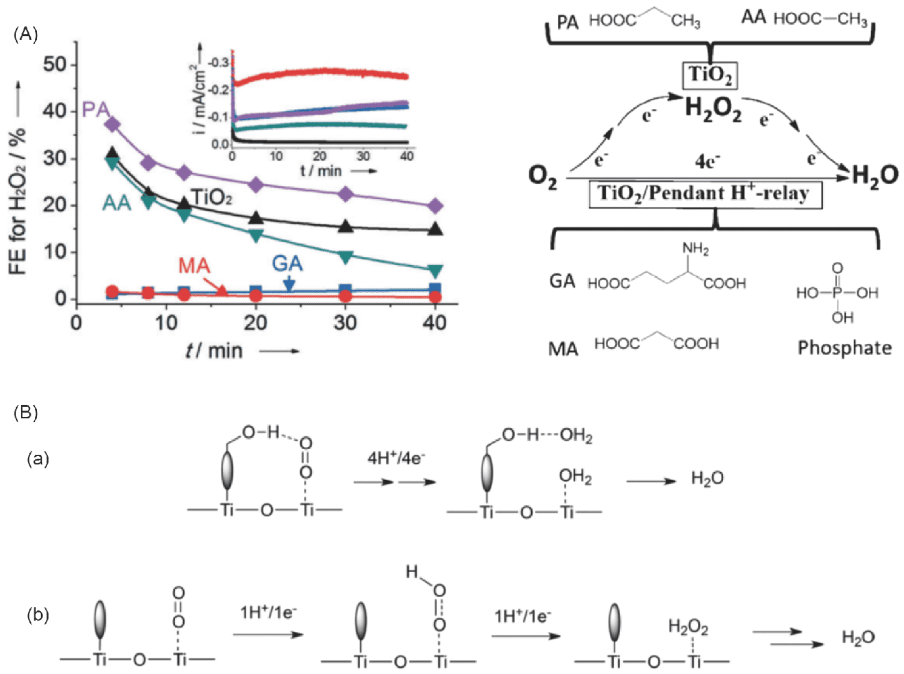

Figure 19 (A) Effect of organic acids on the Faradaic efficiency (FE) for H_2O_2 formation on TiO_2 film during steady-state electrolysis. (B) Mechanism of O_2 reduction on TiO_2 surface with (a) or without (b) pendant proton relays. Reproduced with permission from Ref. [254]. Copyright (2013) Wiley-VCH (color online).

available carboxylic group had been previously used to anchor the molecule to the surface of the catalyst (Figure 19(B), Scheme b). The absence of any significant influence from these monocarboxylic acids on the efficiency of H_2O_2 formation highlighted how important pendant proton relays were in controlling ORR pathways on the TiO_2 surface. On the other hand, after anchoring was completed, a higher local surface proton concentration relative to that seen on pristine TiO_2 surfaces was expected, notwithstanding the fact that the pH values (3.5) were the same as those seen in bulk solutions. This was because the adsorption of carboxylate acid on the TiO_2 surface was dissociative in nature. High surface proton concentrations were responsible for the enhanced reaction rates for O_2 reduction with these acids.

Enhanced multi-electron reduction of O_2 also induced changes in the mechanistic pathway of aromatic photodegradation. With $^{18}O/^{16}O$ isotope labeling to identify the source of the O atoms in the hydroxyl groups of hydroxylated benzoic acids (BA), it was clear that O_2-incorporation was almost eliminated, as evidenced by the decline in the ratio of O_2-sourced O atoms from around 50% on pristine TiO_2 to only 3% in the presence of phosphate. As discussed above, O_2-incoporation required the formation of H_2O_2 intermediates from O_2 reduction reactions to further generate the active species of ·OH [188], which ultimately participated in the oxidation of BA to form BA-OH. Herein, this pathway was shown to contribute equally as the h_{vb}^+-initiated oxidation pathway on pristine TiO_2, since the ratio of O atoms in the hydroxyl group from O_2 or water was almost 1:1. With the addition of pendant proton relays, O_2 did not directly participate in the oxidation of BA, whereas h_{vb}^+ and •OH dominated water oxidation. In this case, O_2 was mainly an electron scavenger with more efficient $4H^+/4e^-$ PCET process to consume electrons, separate the photogenerated carriers, and boost overall efficiency of photodegradation.

The pathway of O_2 reduction was significantly influenced by the surface properties of photocatalysts via the introduction of surface-adsorbed proton relay and increased sensitivity to the exposed crystal facets of the catalysts. O_2-incorporation behavior for a series of anatase TiO_2 samples with controlled percentages of {001} and {101} facets were tested through $^{18}O/^{16}O$ isotope labeling within the framework of this photocatalytic aromatics-hydroxylation model system [255]. During photodegradation of 2-hydroxyterephthalic acid (TPTA), which was accompanied by a gradual increase in the number of exposed {001} facets from 32% to 63%, the percentage of O_2-incorporated TPTA-OH increased from 19.3% to 25.3% (Figure 20). This meant that the contribution ratio of O_2 to water in the hydroxylation reaction was higher on {001} facets than that on {101} ones. Moreover, the utilization of O_2 was more efficient on {001} facets. More O_2 was consumed during the degradation of equal amounts of TPTA, thus, more degradation products were detected on {001} enriched samples.

This result was attributed to the difference in inherent properties between {001} and {101} facets [255]. Firstly, the

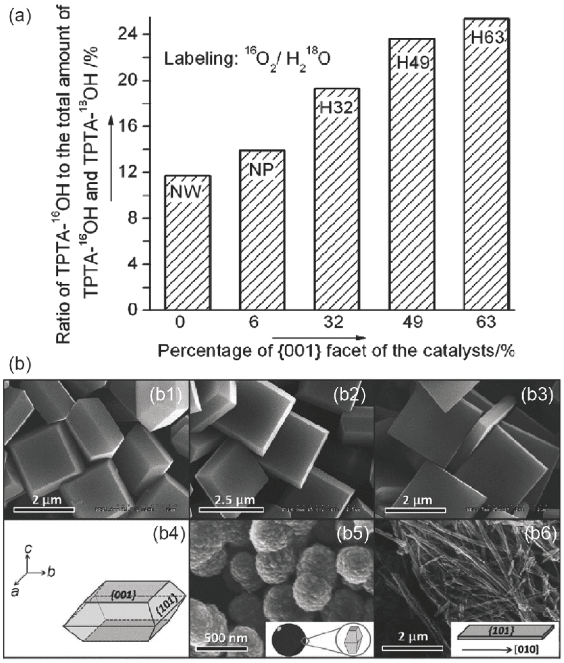

Figure 20 The ratio of O_2-incorporation in the hydroxylation products of TPTA-OH corresponding to the TiO_2 photocatalysts with different ratios of exposed {001} facets. Reproduced with permission from Ref. [255]. Copyright (2012) Wiley-VCH.

conduction band of {101} was 0.04 V more negative than that of {001}, leading to faster electron transfer on {101} [256,82]. Additionally, all the Ti atoms on {001} were unsaturated five-coordinate ones, whereas only half of those on {101} were five-coordinate complexes. As such, the absorption energy of O_2 and water on {001} and {101} was noticeably different [257]. Water molecules were favorably adsorbed onto anatase {101} facet, but adsorption on {001} facets were dissociative and led to the formation of terminal OH and bridged OH pairs [258,259]. As demonstrated both experimentally and in theory, dissociated water molecules had a long-range effect on O_2 adsorption and facilitate O_2 adsorption on {001} facets [260,261]. Therefore, preferable adsorption of the dioxygen, together with the low rate in producing photoinduced electrons, resulted in the formation of more •OH on the {001} facet. This, in turn, led to the incorporation of more dioxygen-derived O atoms into the substrate on the {001} facet.

4.2 Water activation in semiconductor photocatalysis

Water oxidation mainly contributed in two key elements in photocatalytic reactions. The first was the single-hole oxidation of water which served as the main route toward generating ·OH (Eq. (6)), one of the primary oxidants in the photodegradation of organic pollutants. The second was the oxidation of water to O_2 via a half reaction to close the active cycle in artificial photosynthesis or water-splitting reactions; the sluggish kinetics associated with this series of multi-step oxidations made it the rate-limiting step of the entire reaction [262]. Due to their critical roles in photocatalytic and photoelectrocatalytic reactions, water oxidation catalysts with high reaction efficiencies have been of great interest to researchers [263–265]. In this section, the mechanistic approaches through which catalyst surface properties affected the reaction pathways for water oxidation processes are discussed. Theoretical guides for these mechanistic strategies are examined.

It was theorized that water oxidation on TiO_2 photocatalyst was initiated by h_{vb}^+ which had been trapped by molecular water or OH^- adsorbed onto the surface Ti sites (i.e., the terminal OH in five-coordinated Ti_{5c} complex). This was done to generate ·OH. The coupling between two ·OH produced H_2O_2 which was then oxidized to O_2 by h_{vb}^+. It was long believed that the oxidation of surface-adsorbed water species resulted in Ti-O· where the photogenerated holes were entrenched [266,267]. Recently, it was reported that the occupied states of the O 2p orbitals of these adsorbed water species (both molecular water and OH^-) were well below the top edge of the valence band for TiO_2. This was based on both theoretical calculations and photoelectron spectroscopy results [268,269]. As such, transferring h_{vb}^+ to these species was thermodynamically hindered on the perfect TiO_2 surface. This was believed to be the reason behind the sluggish kinetics associated with water oxidation on TiO_2.

To release entrenched h_{vb}^+ from the surface states, one strategy employed by researchers was to modify the surface of TiO_2 with redox-innocent and highly electronegative anions such as F^-, phosphate, sulfate, and naffion [255,270]. These anions were specifically adsorbed onto the surface of TiO_2, thereby replacing the surface terminal OH and forming hydrogen bonds with out-sphere water molecules. Since the strongly adsorbed anions occupied the surface Ti sites and blocked surficial oxidation with water or other organic substrates via h_{vb}^+, hydrogen bonding with the adsorbed anions was used as a means of water activation on TiO_2. The generation of free ·OH (Eq. (6)) was dramatically enhanced and the photodegradation of ·OH-sensitive organic substrates like aromatics were notably more intense [271]. Based on preliminary theoretical calculations, an "anion effect" was proposed which originated from a common mechanism rooted in anion-derived surface negative charges. These charges encouraged the creation of photogenerated holes in the surface of TiO_2 via electro-static forces, and consequently enhanced oxidation of surface-adsorbed species [271]. As a result, ·OH-sensitive organic pollutants such as benzoic acid, benzene, and phenol underwent more rapid degradation, whereas degradation for those less susceptible to ·OH, such as formic acid, were hindered due to the weakened adsorption on the surface.

The strategy of using surface modifications to accelerate interfacial h_{vb}^+ transfers to adsorbed water molecules was also applied to other metal oxide photocatalysts. Hematite is a promising material for PEC water splitting because of its distinct merits, such as an ideal optical band gap (1.9–2.2 eV), high natural abundance, and good stability. However, its application was limited by short hole diffusion lengths and low electron mobility [272]. Even with the assistance in bias, mobility of the photogenerated carriers on hematite remained very low. This threaten to be a major obstacle for efficient light-driven water oxidation, considering that multi-hole oxidation of water required high h_{vb}^+ densities on the surface. To solve this problem, Zhang and co-workers [273] introduced phosphate into the hematite photoanode for efficient solar water splitting. Similar with TiO_2, phosphate interacted strongly with hematite surfaces, providing countless opportunities for introducing doped phosphate onto the surface layer of the hematite under mild conditions. *In situ* formation of the $FeO_x(PO_4)_y$ layer on the outermost sections of the surface was characterized by the presence of a unique gradient structure with a thickness of 50 nm. This surface-doped hematite exhibited vastly improved PEC water oxidation performance; an 8.5-fold increase in the photocurrent density at 1.23 V vs. RHE was achieved when compared to the values observed for the pristine anode. Clearly, enhancement did not shift the onset potential, as was observed when a water oxidation catalyst (WOC, i.e., $CoPO_4$) was added as a co-catalyst, since the mechanism governing this reaction was not simply a catalytic function of $FeO_x(PO_4)_y$. Some common points regarding the "anion effect" on TiO_2 [271] included the strong electronegative nature of phosphate and the oxygen vacancies generated during surface doping which induced a continuous built-in electric field that permeated the entire doping layer. All carriers that were photogenerated in this layer encountered this electric field, which, in turn, forced h_{vb}^+ to move toward the surface. Consequently, the charge diffusion length was expanded to the depth of the gradient-structured layer (~50 nm), nearly 20 times greater than that observed in the pristine hematite (2–4 nm). This was shown to be a major factor in determining the efficiency of PEC water oxidations [48,273].

The "anion effect" either on TiO_2 or hematite was somehow ascribed to the generation of a built-in negative field. However, this assumption is not a true reflection of the process since anions like phosphate or fluoride tended to interact more strongly to the surface of the metal oxide catalyst than to the water molecules present, resulting in modifications that occupied the surface sites and altered the reaction atmosphere for the water molecules on the surface. These anions also shared strong hydrogen bonds with water molecules or protons and were capable of significantly influencing the adsorption mode of the water molecules as well as surface protonation/deprotonation. In one study, an *in situ* FTIR experiment was carried out to gather detailed experimental evidence of this "anion effect," including insight into its modus operandi by tracing and comparing the surficial adsorption and oxidation of water molecules with or without the anions [274]. The water species that was adsorbed onto TiO_2 (molecular water and surface OH groups) had three characteristic vibrational absorption regions in its infrared spectrum. The sharp bands above 3600 cm^{-1} corresponded to the stretching vibrations of the surface OH groups (υ_{OH}). Specifically, the bands above 3680 cm^{-1} belonged to the terminal OH (OH_t), whereas the ones below 3680 cm^{-1} were attributed to the bridged OH (OH_b). These bands became more evident and well-resolved only when the catalyst's surface was dehydrated. An intricate hydrogen bond network with the out-layer water molecules broadened these bands until there was a gradual merge with the broad bands that extended between ~3500 and ~2500 cm^{-1} which represented hydrogen-bonded water molecules. H–O–H scissor bending vibrations of molecular water (δ_{H_2O}) was located at the region around 1630 cm^{-1}. Besides a distinctive red shift linked to stretching vibrations after hydrogen bonding, a blue shift was observed when the surface-adsorbed water was connected with second layer of water molecules via H···O–H bonds. Additionally, the IR bands for the surface-adsorbed water species were very sensitive to interaction modes. Therefore, *in situ* FTIR served as a powerful tool for exploring the adsorption and photooxidation behavior of water species adsorbed onto photocatalysts.

With the deliberate control of the F^--treatment concentration, surface OH groups (OH_t and OH_b) were substituted by F^-. Three types of surface fluorinated TiO_2 samples were then obtained, as shown in Figure 21: a) substitution of OH_t to form F_t; b) substitution of OH_b to form F_b; and c) substitution of both adjacent OH_t and OH_b [274]. Illumination of the pristine or the fluorinated TiO_2 under inert-gas atmosphere was monitored using *in situ* FTIR spectroscopy. No obvious changes were observed on pristine, OH_t-substituted or OH_b-substituted samples, whereas samples in which the groups were OH_t and OH_b substituted showed clear signs of an increase in the monotonic IR absorption band ranging from 3000 to 1000 cm^{-1}. This was attributed to accumulated e_{cb}^-. Concomitant with e_{cb}^- accumulation was the loss in the bands associated with surface-adsorbed water (Figure 21(A)). *In situ* detection protocols for O_2 and a prominent D/H kinetic isotope effects indicated that this loss was not the result of photoinduced desorption, but rather a product of water oxidation to O_2 in the absence of electron scavengers. In the other words, the water oxidation capabilities of TiO_2 were significantly enhanced after fluorination, enabling it to compete with faster recombination reactions of the photogenerated carriers even in the absence of electron scavengers.

To gain insight into the mechanism by which this occurred,

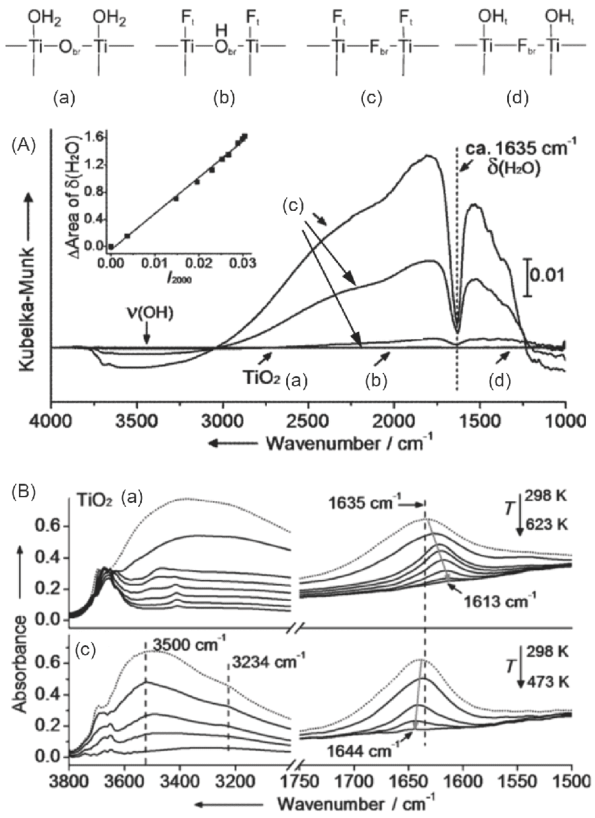

Figure 21 The surface structures of (a) pristine TiO_2 and (b–d) TiO_2 with different fluorination configurations. (A) Change in IR spectra of pristine TiO_2 (a) and TiO_2 with different fluorination configurations. Inset: linear relationship between the area of the negative peak at $1635\ cm^{SCPENC-41-1}$ (δ_{H_2O}) and absorbance at $2000\ cm^{-1}$ (I_{2000}) on sample (c) (both OH_t and OH_b are substituted). (B) Spectra (υ_{OH} and δ_{H_2O} regions) of TiO_2 and the corresponding sample (c) under conditions of water saturation (dashed line) or dehydration at different temperatures. Reproduced with permission from Ref. [274]. Copyright (2015) Wiley-VCH.

the adsorption modes for water molecules on various TiO_2 samples were investigated. On anatase {101} facet, the first layer of water molecules was molecularly adsorbed on Ti_{5c} sites, and the second layer was then connected with the first via a hydrogen bond network. Therefore, the bending vibration observed at ~1630 cm^{-1} was blue shifted with an increase in the number of layers of surface-adsorbed water. Intriguingly, when the adjacent OH_t and OH_b were both substituted, the δ_{H_2O} for the first layer was located at 1644 cm^{-1} with a 31 cm^{-1} blue shift in comparison to that of pristine TiO_2 (1613 cm^{-1}) (Figure 21(B)). With the increase of the number of surface-adsorbed water molecules, δ_{H_2O} values gradually red shifted to 1635 cm^{-1} in contrast to the normal blue shift observed for pristine TiO_2. Due to its strong electronegativity, F^- formed strong hydrogen bonds with water.

Also considering the fact that when only OH_t or OH_b was substituted by F^-, the samples exhibited similar for water adsorption tendencies as those seen for pristine TiO_2. It was concluded that when F^- simultaneously substituted the adjacent OH_t and OH_b on TiO_2, the adsorption mode of first-layer water molecules was changed, and both the adjacent F_t and F_b formed dual hydrogen bonds with the first-layer water molecules. Based on theoretical calculations, this alteration in the water adsorption mode made water activation via these holes thermodynamically possible; however, when water was molecularly adsorbed on Ti_{5c} site, the reaction was thermodynamically forbidden [274]. Dual hydrogen bonds with both H atoms of water restricted the formation of radical intermediates via hole-transfer on the catalyst's surface, thus enabling more efficient multi-hole oxidation of water.

The example of surface fluorination on TiO_2 suggests that the alteration in the adsorption mode of water molecules on TiO_2 significantly changed the behavior of photocatalytic water activation. To consolidate this, another example was prepared with opportunities to compare the activity between the two water adsorption modes. As referred in the last section, two major exposed facets existed in anatase TiO_2: the {101} and {001} facets. It was theoretically proposed that water was molecularly adsorbed on Ti_{5c} sites of the more general {101} facets. However, on {001} facets, adsorption of the first-layer water were considered to be too dissociative to generate the terminal OH_t [258,259] that covered the surface Ti sites. Molecular water could only be adsorbed on these OH_t. This proposition was confirmed using *in situ* FTIR spectroscopy [275]. Two δ_{H_2O} bands were observed when {101} and {001} facets coexisted: one major band at 1615 cm^{-1} and a shoulder at 1647 cm^{-1}. The intensity ratio of these two bands (I_{1647}/I_{1615}) exhibited a positive linear relationship with the ratio of {001} facets exposed. With a higher intensity value at 1647 cm^{-1}, the more prominent band at 3740 cm^{-1} for v_{OH} of OH_t was obtained. The IR band at 1615 cm^{-1} was in accordance with the wavenumber in the last example for molecularly adsorbed water on Ti_{5c} site, and another higher wavenumber for δ_{H_2O} at 1647 cm^{-1} meant that the surficial Ti sites was completely covered by F^-. Thus, these two bands were assigned to two diverse water adsorption modes: the 1615 cm^{-1} bands were associated with molecularly adsorbed water on {101} facets, while the 1647 cm^{-1} bands were for the hydrogen-bonded water molecules of the surface OH groups (OH_t) on the {001} facets [275].

Tracing the photocatalytic water oxidation via *in situ* FTIR [275], it was found that e_{cb}^- accumulation on the photocatalyst was greater when more {001} facets were exposed, as more h_{vb}^+ was consumed by water oxidation. It is worth noting that, during photocatalytic water oxidation, the only reactive water species were the hydrogen-bonded ones on the {001} facet, as no decrease of the number of molecularly adsorbed water on {101} was detected. The decrease of the number of hydrogen-bonded water molecules also induced an increase in the bands of ν_{OH} due to the release of protons from water oxidation which reacted with the surface oxygen sites on TiO_2 to form surface OH groups. Theoretical calculations for this facet-dependent water oxidation coincided with the examples seen during surface fluorination, reinforcing the theory that the bonding of water molecules to TiO_2 surface via hydrogen bonds reduced the activation barrier and allowed for direct h_{vb}^+ transfer. These two examples, together with a similar mechanism for the enhancement of photocatalytic water oxidation, deepened our understanding of the structure-activity relationship and the benefits linked with high efficiency catalysts.

In the *in situ* FTIR studies of excited TiO_2, it was clear that only e_{cb}^- was accumulated on the catalyst during the oxidation half reaction without being consuming by the electron scavengers present. Focusing on the water oxidation reaction simplified the experimental observation and eliminated any interference from the other half reaction. However, e_{cb}^- accumulation intensified the electron-hole recombination, thus limiting further processing of water oxidation. In a PEC cell, e_{cb}^- was transferred to the photocathode through the external bias, which provided a different aspect for the exploration of the water oxidation on photoanode. Sluggish water oxidation kinetics on the surface of hematite was known to be a major efficiency-limiting factor [262], and the mechanistic details for the associated elemental steps remain poorly understood. The challenge lies in the complexity of the coupled $4e^-/4H^+$ process, particularly the simultaneous potential/pH-determined interfacial reaction pathways in the rate-determining step. A thorough understanding of the underlying mechanism for this proton-coupled interfacial electron-transfer process is important for achieving efficient water-splitting reactions by engineering the surface to accelerate the sluggish kinetics.

During water oxidation on hematite photocatalysts, h_{vb}^+ was first trapped on a surface iron species like $\equiv Fe^{III}\text{-}OH$ to form $\equiv Fe^{III}\text{-}O\cdot$, after which additional transfers to the adsorbed water molecules were conducted [276,277]. The pH exhibited significant influence on the water oxidation activities, since OH^- (E_{O_2/OH^-}=0.401 V vs. RHE) was energetically favored than molecular water (E_{O_2/H_2O}=1.229 V vs. RHE). Thus, as shown in Figure 22(A), the photocurrent of water oxidation was very low from pH 7 to 10 (isoelectric point of hematite was around pH 10), under conditions in which the molecular water was the major reactive water species [278]. With the increase in pH accompanied by a rise in the OH^- concentration, the photocurrent of this reaction increased with negative shifting of the onset potential in a Nernstian fashion. Until pH 13 was attained, continuous increases in the photocurrent value without the formation of a plateau indicated that the oxidation of OH^- was the dominant reaction above this pH value. Kinetic isotope studies were conducted in H_2O or D_2O to gain insight into the role of the proton transfer process in the elemental steps of water oxidation (Figure 22(B)). A kinetic isotope effect (KIE) was calculated based on the ratio of the photocurrent in H_2O and D_2O. It was found that KIE was not evident in pH ranges above 12 when OH^- oxidation conditions prevailed. On the other hand, the KIE increased from 2.0 to 3.1 at pH 9.0, with an applied potential between 1.0 and 1.2 V when molecular water was the major participant. Such obvious first-order KIE indicated that cleavage of O–H bonds of molecular water was the rate-determining step that proceeded through a proton-coupled electron-transfer pathway. Here electron transfer occurred simultaneously with the proton transfer process in an effort to break the O–H bonds (Figure 22(C)-a). However, when the pH was higher and the OH^- oxidation reaction dominated, PCET switched to an electron transfer process in which the effect of proton transfer was weakened (Figure 22(C)-b). For the PCET progress in the specific pH range, the addition of surface proton relays, such as borate, phosphate, silicate, and carboxylate, facilitated deprotonation of the water molecules and ultimately induced a significant rise in the PEC performance of water oxidation on hematite [278].

In the mechanistic approach for water oxidation on metal oxides, the most challenging part was detecting the intermediates during the O–O bond formation stage. This was associated with high activation barrier, as indicated by both kinetic studies and theoretical calculations. Two pathways were proposed for homogeneous catalytic systems with a transition-metal complex as the catalyst [279,280]. One pathway proceeded via nucleophilic attack of water/OH^- molecules by a metal-oxo species to form peroxide (WNA pathway) which was further oxidized to O_2. The other pathway was through the coupling of two metal-oxo or oxyl radical species (I2M pathway). *In situ* FTIR spectroscopy was conducted as a means of exploring water oxidation on a metal oxide. Combined with $^{18}O/^{16}O$ isotope labeling, the existence of intermediates like metal peroxide (M-OO^-) or metal-oxo (M=O) during water oxidation was identified. In multi-step reactions like water oxidation, the kinetics of growth and decay of the respective intermediates traced during *in situ* spectral analysis provided additional evidence on the role of the intermediate in the entire water oxidation reaction. Frei and co-workers [281] reported the first direct, temporally resolved observation of surface intermediates for water oxidation on Co_3O_4, one of the most efficient WOC. Using $Ru(bpy)^{3+}$ (bpy=bipyridine) as a photosensitizer to transfer electrons to initiate the water oxidation on Co_3O_4, two intermediates were identified via time-resolved FTIR. One intermediate was attributed to an oxo Co^{IV} site absorbed at 840 cm^{-1}, whereas the other was a surface superoxide absorbed at 1013 cm^{-1}. The temporal behavior of the intermediates revealed that they belonged to different catalytic sites: the Co=O was a one-electron oxidation intermediate, while the Co-OOH was a three-electron oxidized system.

For the PEC system of hematite, Hamann *et al.* [24] also

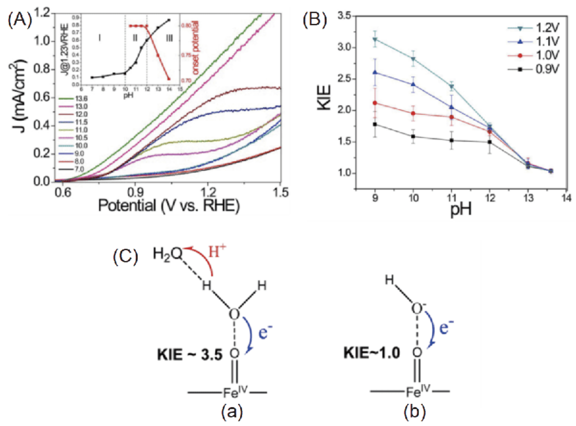

Figure 22 (A) *J-V* scans (50 mV/s) under AM 1.5 G illumination in unbuffered electrolytes (0.5 M $NaClO_4$) at various pH levels. (B) KIE values calculated from the steady photocurrent ratio in H_2O and D_2O for a hematite photoanode in unbuffered electrolyte at various electrolyte pH levels and potentials and under illumination. (C) The mechanism of the electron and proton transfer during interfacial hole transfer for oxidation of (a) H_2O and (b) OH^-. Reproduced with permission from Ref. [278]. Copyright (2013) Wiley-VCH (color online).

reported using *in situ* PEC FTIR spectroscopy for the identification of water oxidation intermediates. The absorption peak at 898 cm^{-1}, which was potential- and light-dependent, was assigned to the Fe^{IV}=O group and was a likely product of first-hole-transfer reactions on the hematite surface. However, the metal peroxide intermediate ($Fe-OO^-$), which was the key intermediate for judging whether the water oxidation went through a WNA or I2M pathway, was not observed in this study.

Based on the combined electrochemical impedance spectroscopy (EIS) and *in situ* FTIR spectroscopy, Zhang and coworkers [282] focused on uncovering distinct O–O bond formation pathways that operated in different pH regions. EIS was applied to determine the reaction orders of the holes trapped on the surface. At pH values of 10.0 and 13.6, the reaction orders were calculated to be 1.1 and 2.4, respectively. A reaction order of 1.1 at pH 10.0 implied the involvement of a single-hole-transfer process during the rate-determining step. This was more likely to follow the WNA pathway in which the transfer of one surface-trapped simultaneously led to the oxidation of Fe=O to FeOOH via a nucleophilic attack by water molecules (Figure 23(A)). In the I2M pathway, on the other hand, the coupling of two adjacent Fe=O to generate O_2 needed a simultaneous two-hole transfer. This theory was supported by the experimental results (2.4 at pH 13.6). It was theorized that this distinct reaction order at different pH originated from surface protonation or hydrogen bond environment that favored different O–O formation pathways.

To further establish the mechanism of O–O bond formation, the surface species generated during PEC water oxidation were monitored via *in situ* FTIR spectroscopy. As

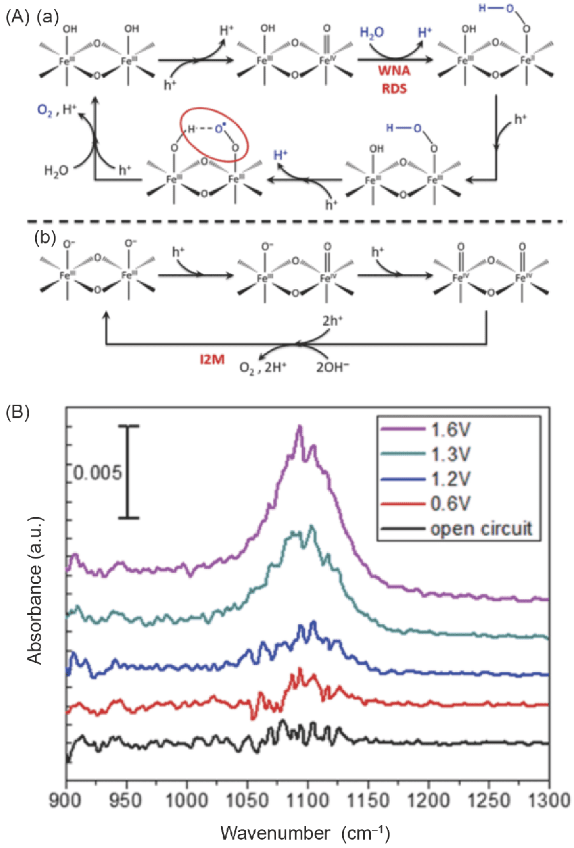

Figure 23 (A) (a) WNA and (b) I2M mechanisms for O–O bond formation on hematite surfaces. (B) FTIR spectra on the hematite photoanode under AM 1.5 G illumination in unbuffered pH 8 electrolyte (0.5 M $NaClO_4$) with applied potentials from 0.6 to 1.6 V vs. RHE. Reproduced with permission from Ref. [282]. Copyright (2018) American Chemical Society (color online).

shown in Figure 23(B), an absorption band at around 1100 cm^{-1} was observed with a bias of 1.3 V vs. RHE in the IR region of the metal peroxide [283]. The isotope shifted after replacing $H_2{}^{16}O$ to $H_2{}^{18}O$ or $D_2{}^{16}O$, consolidating the structure of iron peroxide at 1100 cm^{-1} so that it was not a dangling hydrogenated superoxo molecule. Instead, a hydrogen bond was formed with the adjacent Fe-OH groups that facilitated simultaneous proton transfer coupled with hole transfer as a PCET process. As seen in the EIS results, this 1100 cm^{-1} absorption band gradually disappeared when the pH rose from 8 to 11, confirming once again that in a very alkaline environment, the mechanism by which water oxidation occurred switched from WNA to I2M. This result cemented the notion of an O–O bond formation mechanism in PEC water oxidation on hematite photoanodes and demonstrated the sensitivity of reaction pathways to the interfacial environment.

5 Conclusions

In conclusion, photocatalysis has been extensively studied since the first demonstration of the process half center ago. Redox reactions are useful for a variety of real-world applications, including water-splitting reactions for the production of hydrogen gas as an energy source, CO_2 immobilization to reduce the negative green-house effect, the production of carbohydrates, N_2 fixation for ammonia production, and many more. It has the potential to revolutionize the energy and environmental systems that are based on fossil fuels via the utilization of solar power as a primary energy source. Although progress has been reported in numerous studies, many concerns regarding the field have yet to be properly addressed. For instance, there are still challenges in finding the proper material needed to functionalize as a visible translucent material capable of harvesting most solar incidence. Additionally, issues related to improving the efficiency of the charge separation and transport systems while avoiding recombination reactions that initiate multi-electron redox reactions with sluggish kinetics must be tackled. These and many other findings from the field were summarized in this review, including advances made in the development of charge transport systems for visible-light-sensitive photocatalysts and their underlying surface reaction mechanisms, as well as real-world applications of PCN for photocatalysis. By understanding the synthetic methods, characteristic approaches, and proposed mechanisms that underpin photocatalysis, scientists will be able to eventually overcome the shortcomings associated with these reactions and inspire innovative research aimed at supporting future applications.

Acknowledgements This work was supported by the National Natural Science Foundation of China (21425309, U1905214, 21761132002, 2170304, 21861130353), the National Key Reasearch and Development Program of China (2018YFA0209301), the Chang Jiang Scholars Program of China (T2016147), and the 111 Project (D16008). Yun Zheng thanks the support of the Scientific Research Funds of Huaqiao University (600005-Z17Y0060, 605-50Y17060), the Open Project Program of the State Key Laboratory of Photocatalysis on Energy and Environment of Fuzhou University (SKLPEE-KF201803), the Natural Science Foundation of Fujian Province (2017J01014) and the Graphene Power and Composite Research Center of Fujian Province (2017H2001).

Conflict of interest The authors declare that they have no conflict of interest.

1 Lewis NS, Nocera DG. *Proc Natl Acad Sci USA*, 2006, 103: 15729–15735
2 Schneider J, Matsuoka M, Takeuchi M, Zhang J, Horiuchi Y, Anpo M, Bahnemann DW. *Chem Rev*, 2014, 114: 9919–9986
3 Fujishima A, Honda K. *Nature*, 1972, 238: 37–38
4 Wang S, Lin J, Wang X. *Phys Chem Chem Phys*, 2014, 16: 14656–14660
5 Zhang G, Lan ZA, Wang X. *ChemCatChem*, 2015, 7: 1422–1423
6 Wang S, Wang X. *Appl Catal B-Environ*, 2015, 162: 494–500
7 Wang S, Wang X. *Angew Chem Int Ed*, 2016, 55: 2308–2320
8 Zheng M, Ghosh I, König B, Wang X. *ChemCatChem*, 2019, 11: 703–706
9 Yang C, Huang W, da Silva LC, Zhang KAI, Wang X. *Chem Eur J*, 2018, 24: 17454–17458
10 Zheng M, Shi J, Yuan T, Wang X. *Angew Chem Int Ed*, 2018, 57: 5487–5491
11 Ravelli D, Dondi D, Fagnoni M, Albini A. *Chem Soc Rev*, 2009, 38: 1999–2011
12 Ong WJ, Tan LL, Ng YH, Yong ST, Chai SP. *Chem Rev*, 2016, 116: 7159–7329
13 Lang X, Chen X, Zhao J. *Chem Soc Rev*, 2014, 43: 473–486
14 Wang X, Maeda K, Thomas A, Takanabe K, Xin G, Carlsson JM, Domen K, Antonietti M. *Nat Mater*, 2009, 8: 76–80
15 Zhang G, Zhang M, Ye X, Qiu X, Lin S, Wang X. *Adv Mater*, 2014, 26: 805–809
16 Zhang J, Zhang M, Yang C, Wang X. *Adv Mater*, 2014, 26: 4121–4126
17 Hou Y, Zheng C, Zhu Z, Wang X. *Chem Commun*, 2016, 52: 6888–6891
18 Bardeen J. *Phys Rev*, 1947, 71: 717–727
19 Klahr B, Gimenez S, Fabregat-Santiago F, Hamann T, Bisquert J. *J Am Chem Soc*, 2012, 134: 4294–4302
20 Cummings CY, Marken F, Peter LM, Tahir AA, Wijayantha KGU. *Chem Commun*, 2012, 48: 2027–2029
21 Klahr B, Hamann T. *J Phys Chem C*, 2014, 118: 10393–10399
22 Iandolo B, Hellman A. *Angew Chem Int Ed*, 2014, 53: 13404–13408
23 Yatom N, Neufeld O, Caspary Toroker M. *J Phys Chem C*, 2015, 119: 24789–24795
24 Zandi O, Hamann TW. *Nat Chem*, 2016, 8: 778–783
25 Li C, Luo Z, Wang T, Gong J. *Adv Mater*, 2018, 30: 1707502
26 Le Formal F, Sivula K, Grätzel M. *J Phys Chem C*, 2012, 116: 26707–26720
27 Kuang Y, Yamada T, Domen K. *Joule*, 2017, 1: 290–305
28 Le Formal F, Tétreault N, Cornuz M, Moehl T, Grätzel M, Sivula K. *Chem Sci*, 2011, 2: 737–743
29 Ulman K, Nguyen MT, Seriani N, Gebauer R. *J Chem Phys*, 2016, 144: 094701
30 Xi L, Bassi PS, Chiam SY, Mak WF, Tran PD, Barber J, Chye Loo JS, Wong LH. *Nanoscale*, 2012, 4: 4430–4433
31 Ahn HJ, Yoon KY, Kwak MJ, Jang JH. *Angew Chem Int Ed*, 2016, 55: 9922–9926
32 Jang JW, Du C, Ye Y, Lin Y, Yao X, Thorne J, Liu E, McMahon G, Zhu J, Javey A, Guo J, Wang D. *Nat Commun*, 2015, 6: 7447
33 Zandi O, Hamann TW. *J Phys Chem Lett*, 2014, 5: 1522–1526
34 Zhang M, Luo W, Zhang N, Li Z, Yu T, Zou Z. *Electrochem Commun*, 2012, 23: 41–43
35 Yang Y, Forster M, Ling Y, Wang G, Zhai T, Tong Y, Cowan AJ, Li Y. *Angew Chem Int Ed*, 2016, 55: 3403–3407
36 Tilley SD, Cornuz M, Sivula K, Grätzel M. *Angew Chem Int Ed*, 2010, 49: 6405–6408
37 Tamirat AG, Su WN, Dubale AA, Chen HM, Hwang BJ. *J Mater Chem A*, 2015, 3: 5949–5961
38 Xi L, Tran PD, Chiam SY, Bassi PS, Mak WF, Mulmudi HK, Batabyal SK, Barber J, Loo JSC, Wong LH. *J Phys Chem C*, 2012, 116: 13884–13889
39 Deng J, Zhong J, Pu A, Zhang D, Li M, Sun X, Lee ST. *J Appl Phys*, 2012, 112: 084312
40 Cao D, Luo W, Li M, Feng J, Li Z, Zou Z. *CrystEngComm*, 2013, 15: 2386–2391
41 Lian X, Yang X, Liu S, Xu Y, Jiang C, Chen J, Wang R. *Appl Surf Sci*, 2012, 258: 2307–2311
42 Ling Y, Wang G, Wheeler DA, Zhang JZ, Li Y. *Nano Lett*, 2011, 11: 2119–2125
43 Zandi O, Hamann TW. *Phys Chem Chem Phys*, 2015, 17: 22485–22503
44 Guo X, Wang L, Tan Y. *Nano Energy*, 2015, 16: 320–328
45 Xie J, Liu W, Xin J, Lei F, Gao L, Qu H, Zhang X, Xie Y. *ChemSusChem*, 2017, 10: 4465–4471
46 Yoon KY, Ahn HJ, Kwak MJ, Kim SI, Park J, Jang JH. *J Mater Chem A*, 2016, 4: 18730–18736

47 Kim JY, Magesh G, Youn DH, Jang JW, Kubota J, Domen K, Lee JS. *Sci Rep*, 2013, 3: 2681
48 Zhang Y, Jiang S, Song W, Zhou P, Ji H, Ma W, Hao W, Chen C, Zhao J. *Energy Environ Sci*, 2015, 8: 1231–1236
49 Kaouk A, Ruoko TP, Pyeon M, Gönüllü Y, Kaunisto K, Lemmetyinen H, Mathur S. *J Phys Chem C*, 2016, 120: 28345–28353
50 Ling YC, Wang GM, Reddy J, Wang CC, Zhang JZ, Li Y. *Angew Chem Int Ed*, 2012, 124: 4150–4155
51 Peerakiatkhajohn P, Yun JH, Chen H, Lyu M, Butburee T, Wang L. *Adv Mater*, 2016, 28: 6405–6410
52 Wang Y, Yu T, Chen X, Zhang H, Ouyang S, Li Z, Ye J, Zou Z. *J Phys D-Appl Phys*, 2007, 40: 3925–3930
53 Hou Y, Zuo F, Dagg A, Feng P. *Angew Chem Int Ed*, 2013, 52: 1248–1252
54 Miao C, Ji S, Xu G, Liu G, Zhang L, Ye C. *ACS Appl Mater Interfaces*, 2012, 4: 4428–4433
55 Sivula K, Formal FL, Gratzel M. *Chem Mater*, 2009, 21: 2862–2867
56 Fang T, Guo Y, Cai S, Zhang N, Hu Y, Zhang S, Li Z, Zou Z. *Nanotechnology*, 2017, 28: 394003
57 Li J, Meng F, Suri S, Ding W, Huang F, Wu N. *Chem Commun*, 2012, 48: 8213–8215
58 Zhang N, Guo Y, Wang X, Zhang S, Li Z, Zou Z. *Dalton Trans*, 2017, 46: 10673–10677
59 Zhang Y, Zhang N, Wang T, Huang H, Chen Y, Li Z, Zou Z. *Appl Catal B-Environ*, 2019, 245: 410–419
60 Christoforidis KC, Montini T, Bontempi E, Zafeiratos S, Jaén JJD, Fornasiero P. *Appl Catal B-Environ*, 2016, 187: 171–180
61 Guo Y, Fu Y, Liu Y, Shen S. *RSC Adv*, 2014, 4: 36967–36972
62 Cai J, Li S, Qin G. *Appl Surf Sci*, 2019, 466: 92–98
63 Guo Y, Zhang N, Wang X, Qian Q, Zhang S, Li Z, Zou Z. *J Mater Chem A*, 2017, 5: 7571–7577
64 Zhu X, Guijarro N, Liu Y, Schouwink P, Wells RA, Le Formal F, Sun S, Gao C, Sivula K. *Adv Mater*, 2018, 30: 1801612
65 Shehzad N, Tahir M, Johari K, Murugesan T, Hussain M. *J CO_2 Utiliz*, 2018, 26: 98–122
66 Kočí K, Obalová L, Matějová L, Plachá D, Lacný Z, Jirkovský J, Šolcová O. *Appl Catal B-Environ*, 2009, 89: 494–502
67 Hu J, Odom TW, Lieber CM. *Acc Chem Res*, 1999, 32: 435–445
68 Yuan YJ, Yu ZT, Chen XY, Zhang JY, Zou ZG. *Chem Eur J*, 2011, 17: 12891–12895
69 Ping G, Wang C, Chen D, Liu S, Huang X, Qin L, Huang Y, Shu K. *J Solid State Electrochem*, 2013, 17: 2503–2510
70 Xu H, Ouyang S, Li P, Kako T, Ye J. *ACS Appl Mater Interfaces*, 2013, 5: 1348–1354
71 Cao S, Low J, Yu J, Jaroniec M. *Adv Mater*, 2015, 27: 2150–2176
72 Wang T, Meng X, Liu G, Chang K, Li P, Kang Q, Liu L, Li M, Ouyang S, Ye J. *J Mater Chem A*, 2015, 3: 9491–9501
73 Li C, Xue F, Ding E, He X. *Appl Surf Sci*, 2015, 356: 852–861
74 Nasution H, Purnama E, Kosela S, Gunlazuardi J. *Catal Commun*, 2005, 6: 313–319
75 Tahir M, Amin NAS. *Appl Catal B-Environ*, 2015, 162: 98–109
76 Di Valentin C, Pacchioni G. *Catal Today*, 2013, 206: 12–18
77 Zhou W, Fu H. *ChemCatChem*, 2013, 5: 885–894
78 Zhao Z, Fan J, Wang J, Li R. *Catal Commun*, 2012, 21: 32–37
79 Zhang Z, Huang Z, Cheng X, Wang Q, Chen Y, Dong P, Zhang X. *Appl Surf Sci*, 2015, 355: 45–51
80 Zhang Q, Li Y, Ackerman EA, Gajdardziska-Josifovska M, Li H. *Appl Catal A-General*, 2011, 400: 195–202
81 Liu L, Jiang Y, Zhao H, Chen J, Cheng J, Yang K, Li Y. *ACS Catal*, 2016, 6: 1097–1108
82 Pan J, Liu G, Lu GQM, Cheng HM. *Angew Chem Int Ed*, 2011, 50: 2133–2137
83 Ye L, Mao J, Peng T, Zan L, Zhang Y. *Phys Chem Chem Phys*, 2014, 16: 15675–15680
84 Xie K, Umezawa N, Zhang N, Reunchan P, Zhang Y, Ye J. *Energy Environ Sci*, 2011, 4: 4211–4219
85 Zhou H, Guo J, Li P, Fan T, Zhang D, Ye J. *Sci Rep*, 2013, 3: 1667
86 Kwak BS, Kang M. *Appl Surf Sci*, 2015, 337: 138–144
87 Hernández-Uresti DB, Sánchez-Martínez D, Vallejo-Márquez J, Obregón S, Vázquez A. *Res Chem Intermed*, 2019, 45: 2855–2867
88 Park Y, McDonald KJ, Choi KS. *Chem Soc Rev*, 2013, 42: 2321–2337
89 Luo W, Li Z, Yu T, Zou Z. *J Phys Chem C*, 2012, 116: 5076–5081
90 Luo W, Wang Z, Wan L, Li Z, Yu T, Zou Z. *J Phys D-Appl Phys*, 2010, 43: 405402
91 Ng YH, Iwase A, Kudo A, Amal R. *J Phys Chem Lett*, 2010, 1: 2607–2612
92 Hong SJ, Lee S, Jang JS, Lee JS. *Energy Environ Sci*, 2011, 4: 1781–1787
93 Jo WJ, Jang JW, Kong K, Kang HJ, Kim JY, Jun H, Parmar KPS, Lee JS. *Angew Chem Int Ed*, 2012, 51: 3147–3151
94 Luo W, Wang J, Zhao X, Zhao Z, Li Z, Zou Z. *Phys Chem Chem Phys*, 2013, 15: 1006–1013
95 Chakthranont P, Hellstern TR, McEnaney JM, Jaramillo TF. *Adv Energy Mater*, 2017, 7: 1701515
96 Kim JH, Jang JW, Kang HJ, Magesh G, Kim JY, Kim JH, Lee J, Lee JS. *J Catal*, 2014, 317: 126–134
97 Hu Y, Wu Y, Feng J, Huang H, Zhang C, Qian Q, Fang T, Xu J, Wang P, Li Z, Zou Z. *J Mater Chem A*, 2018, 6: 2568–2576
98 Wang S, He T, Yun JH, Hu Y, Xiao M, Du A, Wang L. *Adv Funct Mater*, 2018, 28: 1802685
99 Hu Y, Su Y, Huang H, Qian Q, Guan Z, Feng J, Li Z, Zou Z. *ChemCatChem*, 2015, 7: 2979–2985
100 Kim TW, Choi KS. *Science*, 2014, 343: 990–994
101 Bae D, Seger B, Vesborg PCK, Hansen O, Chorkendorff I. *Chem Soc Rev*, 2017, 46: 1933–1954
102 Lee DK, Choi KS. *Nat Energy*, 2018, 3: 53–60
103 Kuang Y, Jia Q, Ma G, Hisatomi T, Minegishi T, Nishiyama H, Nakabayashi M, Shibata N, Yamada T, Kudo A, Domen K. *Nat Energy*, 2017, 2: 16191
104 Luo W, Yang Z, Li Z, Zhang J, Liu J, Zhao Z, Wang Z, Yan S, Yu T, Zou Z. *Energy Environ Sci*, 2011, 4: 4046–4051
105 Yourey JE, Pyper KJ, Kurtz JB, Bartlett BM. *J Phys Chem C*, 2013, 117: 8708–8718
106 Nam KM, Cheon EA, Shin WJ, Bard AJ. *Langmuir*, 2015, 31: 10897–10903
107 Ye W, Chen F, Zhao F, Han N, Li Y. *ACS Appl Mater Interfaces*, 2016, 8: 9211–9217
108 Gao Y, Hamann TW. *Chem Commun*, 2017, 53: 1285–1288
109 Gaillard N, Chang Y, DeAngelis A, Higgins S, Braun A. *Int J Hydrogen Energy*, 2013, 38: 3166–3176
110 Pilli SK, Deutsch TG, Furtak TE, Brown LD, Turner JA, Herring AM. *Phys Chem Chem Phys*, 2013, 15: 3273–3278
111 Zhang H, Yilmaz P, Ansari JO, Khan FF, Binions R, Krause S, Dunn S. *J Mater Chem A*, 2015, 3: 9638–9644
112 Valenti M, Dolat D, Biskos G, Schmidt-Ott A, Smith WA. *J Phys Chem C*, 2015, 119: 2096–2104
113 Davi M, Drichel A, Mann M, Scholz T, Schrader F, Rokicinska A, Kustrowski P, Dronskowski R, Slabon A. *J Phys Chem C*, 2017, 121: 26265–26274
114 Hill JC, Ping Y, Galli GA, Choi KS. *Energy Environ Sci*, 2013, 6: 2440–2446
115 Liang Q, Guo Y, Zhang N, Qian Q, Hu Y, Hu J, Li Z, Zou Z. *Sci China Mater*, 2018, 61: 1297–1304
116 Kalyanasundaram K, Borgarello E, Duonghong D, Grätzel M. *Angew Chem Int Ed Engl*, 1981, 20: 987–988
117 Kim YK, Park H. *Energy Environ Sci*, 2011, 4: 685–694
118 Wakerley DW, Kuehnel MF, Orchard KL, Ly KH, Rosser TE, Reisner E. *Nat Energy*, 2017, 2: 17021
119 Li H, Zhou Y, Chen L, Luo W, Xu Q, Wang X, Xiao M, Zou Z. *Nanoscale*, 2013, 5: 11933–11939
120 Lei Z, You W, Liu M, Zhou G, Takata T, Hara M, Domen K, Li C. *Chem Commun*, 2003, 17): 2142–2143
121 Shen S, Zhao L, Zhou Z, Guo L. *J Phys Chem C*, 2008, 112: 16148–

16155
122 Mei Z, Ouyang S, Tang DM, Kako T, Golberg D, Ye J. *Dalton Trans*, 2013, 42: 2687–2690
123 Shen S, Chen X, Ren F, Kronawitter CX, Mao SS, Guo L. *Nanoscale Res Lett*, 2011, 6: 290
124 Ding N, Fan Y, Luo Y, Li D, Meng Q. *APL Mater*, 2015, 3: 104417
125 Wen X, Luo W, Guan Z, Huang W, Zou Z. *Nano Energy*, 2017, 41: 18–26
126 Wang J, Zhang P, Song X, Gao L. *RSC Adv*, 2014, 4: 27805–27810
127 Guan Z, Luo W, Xu Y, Tao Q, Wen X, Zou Z. *ACS Appl Mater Interfaces*, 2016, 8: 5432–5438
128 Hu JS, Ren LL, Guo YG, Liang HP, Cao AM, Wan LJ, Bai CL. *Angew Chem Int Ed*, 2005, 44: 1269–1273
129 Chen D, Huang F, Ren G, Li D, Zheng M, Wang Y, Lin Z. *Nanoscale*, 2010, 2: 2062–2064
130 Wu CC, Cho HF, Chang WS, Lee TC. *Chem Eng Sci*, 2010, 65: 141–147
131 Huang D, Persson C. *Chem Phys Lett*, 2014, 591: 189–192
132 Li Z, Luo W, Zhang M, Feng J, Zou Z. *Energy Environ Sci*, 2013, 6: 347–370
133 Wang J, Fang T, Zhang L, Feng J, Li Z, Zou Z. *J Catal*, 2014, 309: 291–299
134 Fan G, Fang T, Wang X, Zhu Y, Fu H, Feng J, Li Z, Zou Z. *iScience*, 2019, 13: 432–439
135 Wang X, Huang H, Fan G, Li Z, Zou Z. *J Phys Chem C*, 2018, 122: 489–494
136 Hara M, Hitoki G, Takata T, Kondo JN, Kobayashi H, Domen K. *Catal Today*, 2003, 78: 555–560
137 Chun WJ, Ishikawa A, Fujisawa H, Takata T, Kondo JN, Hara M, Kawai M, Matsumoto Y, Domen K. *J Phys Chem B*, 2003, 107: 1798–1803
138 Ishikawa A, Takata T, Kondo JN, Hara M, Domen K. *J Phys Chem B*, 2004, 108: 11049–11053
139 Higashi M, Domen K, Abe R. *Energy Environ Sci*, 2011, 4: 4138–4147
140 Feng J, Cao D, Wang Z, Luo W, Wang J, Li Z, Zou Z. *Chem Eur J*, 2014, 20: 16384–16390
141 Chen S, Shen S, Liu G, Qi Y, Zhang F, Li C. *Angew Chem Int Ed*, 2015, 54: 3047–3051
142 Li M, Luo W, Cao D, Zhao X, Li Z, Yu T, Zou Z. *Angew Chem Int Ed*, 2013, 52: 11016–11020
143 Zhen C, Wang L, Liu G, Lu GQM, Cheng HM. *Chem Commun*, 2013, 49: 3019–3021
144 Su Z, Wang L, Grigorescu S, Lee K, Schmuki P. *Chem Commun*, 2014, 50: 15561–15564
145 Cong Y, Park HS, Wang S, Dang HX, Fan FF, Mullins CB, Bard AJ. *J Phys Chem C*, 2012, 116: 14541–14550
146 Shi Z, Feng J, Shan H, Wang X, Xu Z, Huang H, Qian Q, Yan S, Zou Z. *Appl Catal B-Environ*, 2018, 237: 665–672
147 Suzuki S, Teshima K, Yubuta K, Ito S, Moriya Y, Takata T, Shishido T, Domen K, Oishi S. *CrystEngComm*, 2012, 14: 7178–7183
148 Liu G, Shi J, Zhang F, Chen Z, Han J, Ding C, Chen S, Wang Z, Han H, Li C. *Angew Chem Int Ed*, 2014, 53: 7295–7299
149 Fang T, Huang H, Feng J, Hu Y, Guo Y, Zhang S, Li Z, Zou Z. *Sci Bull*, 2018, 63: 1404–1410
150 Kerlau M, Merdrignac-Conanec O, Guilloux-Viry M, Perrin A. *Solid State Sci*, 2004, 6: 101–107
151 Narkeviciute I, Chakthranont P, Mackus AJM, Hahn C, Pinaud BA, Bent SF, Jaramillo TF. *Nano Lett*, 2016, 16: 7565–7572
152 Ritala M, Kalsi P, Riihelä D, Kukli K, Leskelä M, Jokinen J. *Chem Mater*, 1999, 11: 1712–1718
153 Hajibabaei H, Zandi O, Hamann TW. *Chem Sci*, 2016, 7: 6760–6767
154 Yokoyama D, Hashiguchi H, Maeda K, Minegishi T, Takata T, Abe R, Kubota J, Domen K. *Thin Solid Films*, 2011, 519: 2087–2092
155 Abe R, Takata T, Sugihara H, Domen K. *Chem Lett*, 2005, 34: 1162–1163
156 Abe R, Higashi M, Domen K. *J Am Chem Soc*, 2010, 132: 11828–11829
157 Allam NK, Shaheen BS, Hafez AM. *ACS Appl Mater Interfaces*, 2014, 6: 4609–4615
158 Pei L, Xu Z, Yan S, Zou Z. *J Mater Chem A*, 2017, 5: 12848–12855
159 Gao H, Zhao M, Yan S, Zhou P, Li Z, Zou Z, Liu Q. *RSC Adv*, 2016, 6: 86240–86244
160 Higashi M, Domen K, Abe R. *J Am Chem Soc*, 2012, 134: 6968–6971
161 Feng J, Huang H, Fang T, Wang X, Yan S, Luo W, Yu T, Zhao Y, Li Z, Zou Z. *Adv Funct Mater*, 2019, 29: 1808389
162 Balaz S, Porter SH, Woodward PM, Brillson LJ. *Chem Mater*, 2013, 25: 3337–3343
163 Kim YI. *Ceram Int*, 2014, 40: 5275–5281
164 Kim YI, Woodward PM, Baba-Kishi KZ, Tai CW. *Chem Mater*, 2004, 16: 1267–1276
165 Higashi M, Abe R, Teramura K, Takata T, Ohtani B, Domen K. *Chem Phys Lett*, 2008, 452: 120–123
166 Kim YI. *Ceram Int*, 2012, 38: 2609–2612
167 Günther E, Hagenmayer R, Jansen M. *Z Anorg Allg Chem*, 2000, 626: 1519–1525
168 Mizuno Y, Wagata H, Yubuta K, Zettsu N, Oishi S, Teshima K. *CrystEngComm*, 2013, 15: 8133–8138
169 Park NY, Kim YI. *J Mater Sci*, 2012, 47: 5333–5340
170 Zhang L, Song Y, Feng J, Fang T, Zhong Y, Li Z, Zou Z. *Int J Hydrogen Energy*, 2014, 39: 7697–7704
171 Higashi M, Domen K, Abe R. *J Am Chem Soc*, 2013, 135: 10238–10241
172 Feng J, Luo W, Fang T, Lv H, Wang Z, Gao J, Liu W, Yu T, Li Z, Zou Z. *Adv Funct Mater*, 2014, 24: 3535–3542
173 Zhong Y, Li Z, Zhao X, Fang T, Huang H, Qian Q, Chang X, Wang P, Yan S, Yu Z, Zou Z. *Adv Funct Mater*, 2016, 26: 7156–7163
174 Li Z, Feng J, Yan S, Zou Z. *Nano Today*, 2015, 10: 468–486
175 Eisenberg D, Ahn HS, Bard AJ. *J Am Chem Soc*, 2014, 136: 14011–14014
176 Huang H, Feng J, Fu H, Zhang B, Fang T, Qian Q, Huang Y, Yan S, Tang J, Li Z, Zou Z. *Appl Catal B-Environ*, 2018, 226: 111–116
177 Haydous F, Si W, Guzenko VA, Waag F, Pomjakushina E, El Kazzi M, Sévery L, Wokaun A, Pergolesi D, Lippert T. *J Phys Chem C*, 2019, 123: 1059–1068
178 Zheng Y, Pan Z, Wang X. *Chin J Catal*, 2013, 34: 524–535
179 Wang H, Zhang L, Chen Z, Hu J, Li S, Wang Z, Liu J, Wang X. *Chem Soc Rev*, 2014, 43: 5234–5244
180 Zhang J, Zhang M, Lin S, Fu X, Wang X. *J Catal*, 2014, 310: 24–30
181 Zhang J, Chen Y, Wang X. *Energy Environ Sci*, 2015, 8: 3092–3108
182 Li XH, Wang X, Antonietti M. *Chem Sci*, 2012, 3: 2170–2174
183 Lei Y, Jia H, He W, Zhang Y, Mi L, Hou H, Zhu G, Zheng Z. *J Am Chem Soc*, 2012, 134: 17392–17395
184 Zhang J, Grzelczak M, Hou Y, Maeda K, Domen K, Fu X, Antonietti M, Wang X. *Chem Sci*, 2012, 3: 443–446
185 Zhang J, Zhang M, Sun RQ, Wang X. *Angew Chem Int Ed*, 2012, 51: 10145–10149
186 Chen Y, Zhang J, Zhang M, Wang X. *Chem Sci*, 2013, 4: 3244–3248
187 Lin Z, Wang X. *ChemSusChem*, 2014, 7: 1547–1550
188 Zhang J, Chen X, Takanabe K, Maeda K, Domen K, Epping J , Fu X, Antonietti M, Wang X. *Angew Chem Int Ed*, 2010, 49: 441–444
189 Zheng H-R, Zhang J-S, Wang X-C, Fu X-Z. *Acta Physico-Chim Sin*, 2012, 28: 2336–2342
190 Niu P, Yin LC, Yang YQ, Liu G, Cheng HM. *Adv Mater*, 2014, 26: 8046–8052
191 Lin L, Yu Z, Wang X. *Angew Chem Int Ed*, 2019, 58: 6164–6175
192 Zhou M, Wang S, Yang P, Luo Z, Yuan R, Asiri AM, Wakeel M, Wang X. *Chem Eur J*, 2018, 24: 18529–18534
193 Liu P, Sun N, Liang Y, Chen F. *Res Chem Intermed*, 2018, 44: 843–857
194 Zheng D, Pang C, Liu Y, Wang X. *Chem Commun*, 2015, 51: 9706–9709
195 Maeda K, Kuriki R, Zhang M, Wang X, Ishitani O. *J Mater Chem A*,

2014, 2: 15146–15151
196 Lin L, Ou H, Zhang Y, Wang X. *ACS Catal*, 2016, 6: 3921–3931
197 Zhang H, Lin J, Li Z, Li T, Jia X, Wu XL, Hu S, Lin H, Chen J, Zhu J. *Catal Sci Technol*, 2019, 9: 502–508
198 Ou H, Lin L, Zheng Y, Yang P, Fang Y, Wang X. *Adv Mater*, 2017, 29: 1700008
199 Yu Y, Yan W, Wang X, Li P, Gao W, Zou H, Wu S, Ding K. *Adv Mater*, 2018, 30: 1705060
200 Ou H, Chen X, Lin L, Fang Y, Wang X. *Angew Chem Int Ed*, 2018, 57: 8729–8733
201 Yu H, Shi R, Zhao Y, Bian T, Zhao Y, Zhou C, Waterhouse GIN, Wu LZ, Tung CH, Zhang T. *Adv Mater*, 2017, 29: 1605148
202 Yang P, Zhuzhang H, Wang R, Lin W, Wang X. *Angew Chem Int Ed*, 2019, 58: 1134–1137
203 Yang P, Wang R, Zhou M, Wang X. *Angew Chem Int Ed*, 2018, 57: 8674–8677
204 Mane GP, Talapaneni SN, Lakhi KS, Ilbeygi H, Ravon U, Al-Bahily K, Mori T, Park DH, Vinu A. *Angew Chem Int Ed*, 2017, 56: 8481–8485
205 Ou H, Yang P, Lin L, Anpo M, Wang X. *Angew Chem Int Ed*, 2017, 56: 10905–10910
206 Yang P, Ou H, Fang Y, Wang X. *Angew Chem Int Ed*, 2017, 56: 3992–3996
207 Xiao Y, Tian G, Li W, Xie Y, Jiang B, Tian C, Zhao D, Fu H. *J Am Chem Soc*, 2019, 141: 2508–2515
208 Yang C, Wang B, Zhang L, Yin L, Wang X. *Angew Chem Int Ed*, 2017, 56: 6627–6631
209 Fang Y, Li X, Wang X. *ACS Catal*, 2018, 8: 8774–8780
210 Fang Y, Li X, Wang X. *ChemSusChem*, 2019, 12: 2605–2608
211 Ruan Q, Luo W, Xie J, Wang Y, Liu X, Bai Z, Carmalt CJ, Tang J. *Angew Chem Int Ed*, 2017, 56: 8221–8225
212 Fang Y, Xu Y, Li X, Ma Y, Wang X. *Angew Chem Int Ed*, 2018, 57: 9749–9753
213 Bojdys MJ, Müller JO, Antonietti M, Thomas A. *Chem Eur J*, 2008, 14: 8177–8182
214 Lin L, Wang C, Ren W, Ou H, Zhang Y, Wang X. *Chem Sci*, 2017, 8: 5506–5511
215 Lin L, Ren W, Wang C, Asiri AM, Zhang J, Wang X. *Appl Catal B-Environ*, 2018, 231: 234–241
216 Zhang G, Li G, Lan ZA, Lin L, Savateev A, Heil T, Zafeiratos S, Wang X, Antonietti M. *Angew Chem*, 2017, 129: 13630–13634
217 Zhang G, Li G, Heil T, Zafeiratos S, Lai F, Savateev A, Antonietti M, Wang X. *Angew Chem Int Ed*, 2019, 58: 3433–3437
218 Chen Z, Savateev A, Pronkin S, Papaefthimiou V, Wolff C, Willinger MG, Willinger E, Neher D, Antonietti M, Dontsova D. *Adv Mater*, 2017, 29: 1700555
219 Peng G, Albero J, Garcia H, Shalom M. *Angew Chem Int Ed*, 2018, 57: 15807–15811
220 Navarro-Aguilar AI, Obregón S, Hernández-Uresti DB, Suárez-de la Cruz J. *Res Chem Intermed*, 2019, 45: 3865–3878
221 Zheng D, zhang G, Wang X. *Appl Catal B-Environ*, 2015, 179: 479–488
222 Wang Y, Liu X, Liu J, Han B, Hu X, Yang F, Xu Z, Li Y, Jia S, Li Z, Zhao Y. *Angew Chem Int Ed*, 2018, 57: 5765–5771
223 Yu J, Lei J, Wang L, Guillard C, Zhang J, Liu Y, Anpo M. *Res Chem Intermed*, 2019, 45: 4237–4247
224 Huang P, Huang J, Pantovich SA, Carl AD, Fenton TG, Caputo CA, Grimm RL, Frenkel AI, Li G. *J Am Chem Soc*, 2018, 140: 16042–16047
225 Pan Z, Zhang G, Wang X. *Angew Chem Int Ed*, 2019, 58: 7102–7106
226 Wang X. *ChemSusChem*, 2018, 11: 327–329
227 Jiang Z, Wan W, Li H, Yuan S, Zhao H, Wong PK. *Adv Mater*, 2018, 30: 1706108
228 Qiu P, Xu C, Zhou N, Chen H, Jiang F. *Appl Catal B-Environ*, 2018, 221: 27–35
229 Wang Y, Bai L, Zhang Z, Qu Y, Jing L. *Res Chem Intermed*, 2019, 45: 249–259
230 Zhang M, Luo Z, Zhou M, Zhang G, Alamry KA, Taib LA, Asiri AM, Wang X. *Appl Catal B-Environ*, 2017, 210: 454–461
231 Yang J, Wang D, Han H, Li C. *Acc Chem Res*, 2013, 46: 1900–1909
232 Indra A, Acharjya A, Menezes PW, Merschjann C, Hollmann D, Schwarze M, Aktas M, Friedrich A, Lochbrunner S, Thomas A, Driess M. *Angew Chem Int Ed*, 2017, 56: 1653–1657
233 Cao Y, Chen S, Luo Q, Yan H, Lin Y, Liu W, Cao L, Lu J, Yang J, Yao T, Wei S. *Angew Chem Int Ed*, 2017, 56: 12191–12196
234 Zhang L, Yang C, Xie Z, Wang X. *Appl Catal B-Environ*, 2018, 224: 886–894
235 Zheng D, Cao XN, Wang X. *Angew Chem Int Ed*, 2016, 55: 11512–11516
236 Zhou Y, Zhang L, Wang W. *Nat Commun*, 2019, 10: 506
237 Cai J, Huang J, Wang S, Iocozzia J, Sun Z, Sun J, Yang Y, Lai Y, Lin Z. *Adv Mater*, 2019, 31: 1806314
238 Chen R, Pang S, An H, Zhu J, Ye S, Gao Y, Fan F, Li C. *Nat Energy*, 2018, 3: 655–663
239 Lang X, Ma W, Chen C, Ji H, Zhao J. *Acc Chem Res*, 2014, 47: 355–363
240 Migliore A, Polizzi NF, Therien MJ, Beratan DN. *Chem Rev*, 2014, 114: 3381–3465
241 Huynh MHV, Meyer TJ. *Chem Rev*, 2007, 107: 5004–5064
242 Weinberg DR, Gagliardi CJ, Hull JF, Murphy CF, Kent CA, Westlake BC, Paul A, Ess DH, McCafferty DG, Meyer TJ. *Chem Rev*, 2012, 112: 4016–4093
243 Li Y, Wen B, Ma W, Chen C, Zhao J. *Environ Sci Technol*, 2012, 46: 5093–5099
244 Bui TD, Kimura A, Ikeda S, Matsumura M. *J Am Chem Soc*, 2010, 132: 8453–8458
245 Czili H, Horváth A. *Appl Catal B-Environ*, 2008, 81: 295–302
246 Li Y, Wen B, Yu C, Chen C, Ji H, Ma W, Zhao J. *Chem Eur J*, 2012, 18: 2030–2039
247 Hoffmann MR, Martin ST, Choi W, Bahnemann DW. *Chem Rev*, 1995, 95: 69–96
248 Carraway ER, Hoffman AJ, Hoffmann MR. *Environ Sci Technol*, 1994, 28: 786–793
249 Schwitzgebel J, Ekerdt JG, Gerischer H, Heller A. *J Phys Chem*, 1995, 99: 5633–5638
250 Fox MA, Chen CC, Younathan JNN. *J Org Chem*, 1984, 49: 1969–1974
251 Pang X, Chang W, Chen C, Ji H, Ma W, Zhao J. *J Am Chem Soc*, 2014, 136: 8714–8721
252 Valdez CN, Braten M, Soria A, Gamelin DR, Mayer JM. *J Am Chem Soc*, 2013, 135: 8492–8495
253 Schrauben JN, Hayoun R, Valdez CN, Braten M, Fridley L, Mayer JM. *Science*, 2012, 336: 1298–1301
254 Sheng H, Ji H, Ma W, Chen C, Zhao J. *Angew Chem Int Ed*, 2013, 52: 9686–9690
255 Zhao Y, Ma W, Li Y, Ji H, Chen C, Zhu H, Zhao J. *Angew Chem Int Ed*, 2012, 51: 3188–3192
256 Li YF, Liu ZP, Liu LL, Gao W. *J Am Chem Soc*, 2010, 132: 13008–13015
257 Lazzeri M, Vittadini A, Selloni A. *Phys Rev B*, 2001, 63: 155409
258 Blomquist J, Walle LE, Uvdal P, Borg A, Sandell A. *J Phys Chem C*, 2008, 112: 16616–16621
259 Sumita M, Hu C, Tateyama Y. *J Phys Chem C*, 2010, 114: 18529–18537
260 Yang D, Liu H, Zheng Z, Yuan Y, Zhao JC, Waclawik ER, Ke X, Zhu H. *J Am Chem Soc*, 2009, 131: 17885–17893
261 Liu LM, McAllister B, Ye HQ, Hu P. *J Am Chem Soc*, 2006, 128: 4017–4022
262 Tang J, Durrant JR, Klug DR. *J Am Chem Soc*, 2008, 130: 13885–13891
263 Woodhouse M, Parkinson BA. *Chem Soc Rev*, 2009, 38: 197–210
264 Qu Y, Duan X. *Chem Soc Rev*, 2013, 42: 2568–2580
265 Youngblood WJ, Lee SHA, Maeda K, Mallouk TE. *Acc Chem Res*, 2009, 42: 1966–1973

266 Minero C, Mariella G, Maurino V, Pelizzetti E. *Langmuir*, 2000, 16: 2632–2641
267 Bahnemann DW, Hilgendorff M, Memming R. *J Phys Chem B*, 1997, 101: 4265–4275
268 Nakamura R, Nakato Y. *J Am Chem Soc*, 2004, 126: 1290–1298
269 Salvador P. *J Phys Chem C*, 2007, 111: 17038–17043
270 Wang Q, Chen C, Zhao D, Ma W, Zhao J. *Langmuir*, 2008, 24: 7338–7345
271 Sheng H, Li Q, Ma W, Ji H, Chen C, Zhao J. *Appl Catal B-Environ*, 2013, 138-139: 212–218
272 Sivula K, Le Formal F, Grätzel M. *ChemSusChem*, 2011, 4: 432–449
273 Zhang Y, Zhou Z, Chen C, Che Y, Ji H, Ma W, Zhang J, Song D, Zhao J. *ACS Appl Mater Interfaces*, 2014, 6: 12844–12851
274 Sheng H, Zhang H, Song W, Ji H, Ma W, Chen C, Zhao J. *Angew Chem Int Ed*, 2015, 54: 5905–5909
275 Zhang H, Zhou P, Chen Z, Song W, Ji H, Ma W, Chen C, Zhao J. *J Phys Chem C*, 2017, 121: 2251–2257
276 Klahr B, Gimenez S, Fabregat-Santiago F, Bisquert J, Hamann TW. *Energy Environ Sci*, 2012, 5: 7626–7636
277 Upul Wijayantha KG, Saremi-Yarahmadi S, Peter LM. *Phys Chem Chem Phys*, 2011, 13: 5264–5270
278 Zhang Y, Zhang H, Ji H, Ma W, Chen C, Zhao J. *J Am Chem Soc*, 2016, 138: 2705–2711
279 Shaffer DW, Xie Y, Concepcion JJ. *Chem Soc Rev*, 2017, 46: 6170–6193
280 Romain S, Vigara L, Llobet A. *Acc Chem Res*, 2009, 42: 1944–1953
281 Zhang M, de Respinis M, Frei H. *Nat Chem*, 2014, 6: 362–367
282 Zhang Y, Zhang H, Liu A, Chen C, Song W, Zhao J. *J Am Chem Soc*, 2018, 140: 3264–3269
283 Chen C, Shi T, Chang W, Zhao J. *ChemCatChem*, 2015, 7: 724–731